

**3-D P-WAVE VELOCITY STRUCTURE BENEATH EASTERN TURKEY
APPLYING LOCAL EARTHQUAKE TOMOGRAPHY (LET) METHOD**

by

UĞUR MUSTAFA TEOMAN

B.S., Physics Engineering, Istanbul Technical University

Submitted to

Boğaziçi University

Kandilli Observatory and Earthquake Research Institute

in partial fulfillment of

the requirements for the degree of

Master of Science

in

Geophysics

Bogazici University Library



39001106848362

14

Boğaziçi University

2005

ACKNOWLEDGEMENTS

To start with, I would like to thank my thesis supervisor Prof. Dr. Niyazi Türkelli for his guidance throughout this study, also for sharing his knowledge and experience with me since I began working in Kandilli Observatory. He was encouraging and innovative from many aspects and still is.

I am very grateful to Dr. Rengin Gök for providing me her computer account in Mexico University to run the code properly. I could not have obtained the results otherwise. She also had to deal with my numerous e-mails about the code and the method with patience.

Prof. Dr. Engin Arik from department of Physics gave me a hand at a very crucial time during the data compilation stages. She has worked with us all day long without sleep (even Tuna Eken and I were not thinking clearly after 2.00 am) and eventually figured the problem out. I am really grateful to her, deeply appreciate her attitude and ability to work long hours without losing any concentration.

I would also like to thank all members of the geophysics department especially my colleagues Fatih Bulut, Birsen Can, Tuna Eken and Tuna Şeyhan. Fatih Bulut always helped me with his scientific reviews without hesitation whenever I needed. Birsen Can and Tuna Eken were always encouraging and helpful with their ideas and careful reviews together with Tuna Şeyhan. I'd better refer them as "friends" rather than colleagues and definitely know our relations would go along much further until the end of our lives (as long as they can stay calm and be patient to me actually:-)).

Another long-term friend, Gülce Öğrüç deserves many thanks for being with me through the ups and downs in my life since we have met during the physics lectures in Istanbul Technical University. I feel extremely proud and lucky to have such a close and a permanent friend like her.

The most valuable and sincere thanks go to my whole family, especially my mother for being so helpful, sacrificing, and supportive in every stage of my life.

Uğur Mustafa Teoman

TABLE OF CONTENTS

	<u>Page No</u>
ABBREVIATIONS	iv
LIST OF SYMBOLS	v
LIST OF TABLES	vi
LIST OF FIGURES	vii
SUMMARY	xiii
ÖZET	xv
1. INTRODUCTION	1
2. TECTONIC STRUCTURE OF EASTERN TURKEY AND PREVIOUS STUDIES	2
2.1. Tectonic Structure of Eastern Turkey	7
2.2. Previous Seismic Studies in Eastern Turkey	9
3. STATION NETWORK AND DATA COMPILATION	11
3.1. Initial Earthquake Locations	12
4. DERIVATION OF THE 1-D MINIMUM VELOCITY MODEL FOR LOCAL EARTHQUAKE TOMOGRAPHY (LET)	15
4.1. Coupled Hypocenter Velocity Problem	15
4.2. Concept of the Minimum 1-D Velocity Model	17
4.3. Calculation Steps of the 1-D Initial Velocity Model	18
4.4. Calculation of 1-D Minimum Velocity Model for Eastern Turkey	19
4.5. Stability Tests for the 1-D P-Wave Velocity Model	24
4.5.1. Systematic Shifting Test	25
4.5.2. Random Shifting Test	27

5. THREE DIMENSIONAL (3-D) SEISMIC VELOCITY TOMOGRAPHY	30
5.1. Basic Let Theory	31
5.1.1. Representation of the Velocity Structure	33
5.1.2. Ray-Path and Travel Time Calculation	34
5.1.3. Hypocenter –Velocity Structure Coupling	36
5.1.4. The Method of Inversion And Simulps14 Algorithm	37
5.1.4.1. Model Parameterization in SIMULPS14	38
5.1.5. Solution Quality	40
5.1.6 Use of Shear (S) Waves	41
5.2. 3-D Tomographic Applications for Eastern Turkey	42
5.2.1. Data Selection	42
5.2.2. Model Parameterization	43
5.2.3. Control Parameters	44
5.3. Solution Quality Assessment	44
5.3.1. Resolution Assessment with Synthetic Data	45
5.3.2. Resolution Parameters of Real Data	49
5.4. Results of 3-D Inversions	51
5.5. Final Hypocenter Locations	55
5.6. Interpretation of the 3-D Velocity Structure	57
6. CONCLUSIONS	63
REFERENCES	65

LIST OF ABBREVIATIONS

1-D	: One Dimensional
2-D	: Two Dimensional
3-D	: Three Dimensional
ACH	: Aki-Christoffersson-Huseybe Method
ART	: Algebraic Reconstruction Technique
ART-PB	: Approximate Ray Tracing-Pseudo Bending
BVP	: Boundary Value Problem
DWS	: Derivative Weight Sum
EAFZ	: East Anatolian Fault Zone
ETSE	: Eastern Turkey Seismic Experiment
IVP	: Initial Value Problem
KOERI	: Kandilli Observatory and Earthquake Research Institute
LTA/STA	: Long Term Average/Short Term Average
LET	: Local Earthquake Tomography
NAFZ	: North Anatolian Fault Zone
RDE	: Resolution Diagonal Element
RKP	: Runge-Kutta Perturbations
RMS	: Root Mean Square
SIRT	: Simultaneous Iterative Reconstruction Technique
SVD	: Singular Value Decomposition

LIST OF SYMBOLS

I	: Unity Matrix
M_l	: Local Magnitude
M_w	: Moment Magnitude
R	: Resolution Matrix
C_m	: Covariance Matrix
P	: P-wave
V_p	: P-wave velocity
S	: S-wave
T	: Travel time
V_s	: S-wave velocity
λ	: Damping Factor
t	: Arrival time
u	: Slowness
z	: Depth
r	: Residuals
h	: Hypocentral parameters
s	: Station coordinates
m	: Velocity field
e	: Vector of travel time errors

LIST OF TABLES

	Page No
Table 3.1. Initial 1-D velocity model used in earthquake location procedure.....	12
Table 5.1. One dimensional (1-D) minimum P wave velocity model	43

Figure 2.1 Map showing the major tectonic structure of Eastern Turkey and the surrounding regions (Gök, R. 2000).	7
Figure 2.2 GPS velocity vectors for Eastern Turkey (Reilinger et al, 1997).....	8
Figure 2.3 Map showing the tomographic image of Pn velocity. Blank lines indicate the major faults. Pink lines show the coastlines and green dashed lines represent the national boundaries. (Al Lazki, 2003).	9
Figure 2.4 Map showing Sn efficiency tomography results. Green lines represent the major tectonic boundaries and coastlines; blank lines are national boundaries (Gok et.al., 2003).	10
Figure 3.1 Station geometry of the ETSE seismic network. Big black triangles denote the ETSE stations and the small black triangles denote the local permanent short period stations.....	11
Figure 3.2 Initial earthquake locations and depth distribution along with latitude and longitude depth cross-sections. Yellow triangles represent the stations and red circles represent the events. Blue stars denote two moderate size earthquakes.	13
Figure 3.3 Flow chart and the calculation steps of the study.....	14
Figure 4.1 Events used for the 1-D velocity inversion (yellow circles) with their depth distribution (open yellow circles in both depth cross-sections) and the initial locations (red circles).	20
Figure 4.2 Inversion results for three trial velocity models: (a) with low velocities, (b) with intermediate velocities, and (c) with high velocities. Red line denotes the output and the blue line denotes the input velocity model.....	21

Figure 4.3 Inversion results for the resulting velocity model (blue line) from the previous inversion with three different trial velocity models. Red line represents the output velocity model.....	22
Figure 4.4 Inversion results of the relocated data set with the updated velocity model and the station corrections. Blue line represents the input model and the red line represents the output model.	23
Figure 4.5 1-D Minimum P wave velocity model for Eastern Turkey obtained from the previous velocity inversions (blue line).	23
Figure 4.6 The initial and the final earthquake locations. Red circles denote the initial and the yellow circles denote final event locations. Open yellow circles represent the final event depths. Blue triangles denote the stations..	24
Figure 4.7 Inversion results after applying the constant shifting values for the underdamped velocity values. Red dots denote the shifted hypocenters and the resulting hypocenters are indicated with blue dots. (a) Latitude shift (km) (b) Longitude shift (km) (c) Depth shift (km).....	25
Figure 4.8 Inversion results after applying the constant shifting values for the fixed velocity values. Red dots denote the shifted hypocenters and the resulting hypocenters are indicated with blue dots. (a) Latitude shift (km) (c) Longitude shift (km) (c) Depth shift (km).....	26
Figure 4.9 Inversion results after applying random shifting values for the underdamped velocity values. Red dots denote the shifted hypocenters and the resulting hypocenters are indicated with blue dots. (a) Latitude shift (km) (b) Longitude shift (km) (c) Depth shift (km).....	27

Figure 4.10 Inversion results after applying the constant shifting values for the fixed velocity values. Red dots denote the shifted hypocenters and the resulting hypocenters are indicated with blue dots. (a) Latitude shift (km) (b) Longitude shift (km) (c) Depth shift (km).....	28
Figure 5.1 Schematic representation of the LET problem. Sources are distributed within the model volume.	31
Figure 5.2 Geometry of three different approaches to velocity model representation: (a) constant velocity blocks, (b) laterally varying layers, (c) grid of nodes. Dashed lines indicate the spatial form of interpolation (Thurber, 1993).	34
Figure 5.3 Schematic representation of the two ray tracing techniques: ray shooting (top) and ray bending (bottom).	35
Figure 5.4 Node-grid geometry in SIMULPS14. Grid spacing may not be equal to account for the heterogeneities in the structure.....	39
Figure 5.5 Scheme for 3D cubic B-spline interpolation. The solid black circles are the control values (grid nodes) and the gray circle is the target point. a) Interpolation along z onto x-y plane of point. b) interpolation along y onto x-coordinate of point. c) Interpolation along x onto point.	40
Figure 5.6 Selected event locations for the tomographic inversion along with the depth distribution in latitude and longitude depth cross-sections. Yellow triangles represent the stations, red circles represent the events, plus signs represent the nodes that were held fixed in the inversion and the theoretical ray-paths are shown with gray lines.	42
Figure 5.7 Trade-off curves indicating the model variance versus the data variance after one iteration. From this curve “75” was selected as the appropriate damping value shown with a black arrow.	44

Figure 5.8	Horizontal depth sections of synthetic chequerboard input model. P-wave velocity perturbations are shown relative to the 1-D minimum reference model.	45
Figure 5.9	Horizontal depth sections of inversion results for the synthetic data set. P-wave velocity perturbations are shown relative to the 1-D minimum reference model. Red circles represent the events, yellow triangles represent the stations and black triangles denote the grid nodes used in the inversion.	46
Figure 5.10	Horizontal depth sections of the synthetic velocity model based on the inversion results of the actual earthquake data. P-wave velocity perturbations are shown relative to the 1-D minimum reference model. Black triangles represent the grid nodes.	47
Figure 5.11	Horizontal depth sections of the inversion results for the synthetic resolution test along with the earthquake and station distribution. P-wave velocity perturbations are shown relative to the 1-D minimum reference model. Red circles represent the events, yellow triangles represent the stations and black triangles denote the grid nodes used in the inversion.	48
Figure 5.12	Horizontal depth sections of (a) KHIT and (b) DWS for the final Vp model. Events are shown by red circles, stations are shown by yellow triangles and small crosses denote grid nodes. White contour surrounds the area of reliable resolution (RDEs > 0.2).	49
Figure 5.13	Horizontal depth sections of RDEs for the final Vp model. Events are shown by red circles, stations are shown by yellow triangles and small crosses denote the grid nodes.	50
Figure 5.14	Horizontal plane views of absolute velocity (Vp) distribution for different layers down to 20km. Major faults are shown by black lines. Red circles represent the events and yellow triangles represent the stations.	51

Figure 5.15 Horizontal plane views of V_p perturbations (%) relative to the initial 1-D minimum velocity model for different layers down to 20km. Red circles represent the events and yellow triangles represent the stations. Cells with $RDE > 0.2$ are shown by a white contour.	52
Figure 5.16 Initial and final hypocenter distribution after the 3-D inversion. Red and white circles denote the initial and the final hypocenters with the updated 3-D velocity model, respectively. Yellow triangles represent the stations and the blue lines denote the profiles.	55
Figure 5.17 (a) Horizontal displacement of hypocenters. Blue dots represent the displacement values. (b) Comparison of the earthquake locations from the 1-D minimum velocity model and the 3-D model along 4 profiles (A-A'', B-B'', C-C'' and D-D''). Yellow circles represent the initial locations before the 3-D inversion. Displacement vectors are drawn to the final 3-D locations by thin lines.	56
Figure 5.18 P-wave velocity distribution along three profiles (A-A', B-B', C-C') perpendicular to EAFZ. Areas of higher resolution are surrounded by a white contour ($RDEs > 0.2$). V_p values are contoured in every 0.2 km/sec interval.	58
Figure 5.19 P-wave velocity distribution along three profiles (D-D', E-E', F-F') perpendicular to NAFZ. Areas of higher resolution are surrounded by a white contour ($RDEs > 0.2$). V_p values are contoured in every 0.2-km/sec intervals.	59
Figure 5.20 P-wave velocity distribution along three profiles (G-G', H-H', I-I'). Areas of higher resolution are surrounded by a white contour ($RDEs > 0.2$). V_p values are contoured in every 0.2-km/sec intervals.	60

Figure 5.21 P-wave velocity distribution along three profiles (J-J', K-K'). Areas of higher resolution are surrounded by a white contour (RDEs > 0.2). Vp values are contoured in every 0.2-km/sec intervals.61

SUMMARY

Eastern Turkey is a seismically active region exhibiting a complex structure in terms of both tectonic and geologic features. A temporary seismic network consisting of 29 broadband three-component broadband stations were installed in the scope of Eastern Turkey Seismic Experiment (ETSE) to address the important questions. Detailed and accurate evidences relevant to the crustal and upper mantle structure of the region were obtained using the seismic data collected in between October 1999 and August 2001. Results of the ETSE project had a considerable contribution to understanding and interpreting the tectonic evolution along with the seismicity of the region.

In this study, local earthquake data from the ETSE project were used in order to determine the upper crust seismic P wave velocity structure of Eastern Turkey and the surrounding regions by three-dimensional (3-D) Local Earthquake Tomography (LET) method. As far as resolution is concerned, S waves were not included in this study due to strong attenuation, insufficient number of S phase readings and higher picking errors with respect to P phases.

LET is the 3-D imaging process of the velocity structure of a target volume by using the travel time data of the earthquakes recorded within the seismic network in an active region. To provide accurate tomographic results, a high quality data set, initial hypocentral parameters and a minimum one-dimensional (1-D) velocity model that adequately represents the region are required.

Initially, data compilation and earthquake locations were determined. Initial locations of 944 events were performed by HYPOCENTER algorithm using an initial 1-D velocity model, which was obtained from the previous studies in the region.

Following the earthquake location procedure, higher quality events were selected in order to construct the 1-D minimum velocity model for the region. As a basic data selection criteria, events with azimuthal gap ($GAP \leq 200^\circ$) and number of observations ($P \geq 8$) were selected from the initial data set (6978 P-phase readings). 1-D velocity model was calculated by VELEST algorithm performing a simultaneous and iterative 1-D velocity inversion. New hypocentral parameters and station corrections were also calculated in addition to the minimum velocity model. Three different trial velocity models were used in order to construct an initial velocity model based on the results of a

set of inversions with ten iterations and four calculation steps. Each velocity model were constructed in 0-42 depth range in accordance with the crustal structure of the region, however, accurate results were obtained down to 15-20 km due to the depth distribution of the events. The relocation of the earthquakes was performed by VELEST via the 1-D minimum velocity model and the relevant station corrections. In the final step, various stability tests were applied to check the resolution capability minimum 1-D velocity model. As a result of these tests, it was suggested that 1-D minimum velocity model adequately represented the region.

After the derivation of the most appropriate velocity model, 3-D tomographic inversions were applied to the final data set. Events with $GAP \leq 180^\circ$ and $P > 8$ were reselected from the data set. Number of events for the tomographic inversion reduced to 504 after applying this criteria (Total number of 6742 P-phase readings). 3-D tomographic inversion was iteratively and simultaneously performed by SIMULPS14 algorithm using node-grid geometry for model parameterization. Considering the event-station distribution, a horizontal grid with 30x30 km grid spacing was chosen. In vertical direction, depth values taken from the 1-D velocity model were used. Modeling was made down to 42 km. Tomographic inversions with four iterations and two processing steps were initiated after determining the appropriate control parameters and the damping factor. At the end of these processes, 3-D P wave velocity model and the resulting hypocenters were determined. A significant reduction in data variance ($\sim 50\%$) and in residuals ($\sim 50\%$) was observed during these processes. In order to assess the solution quality and the resolving power of the 3-D model, tests with the synthetic data were performed. Critical parameters affecting the resolution estimates were calculated and mapped along with absolute velocities (V_p) and % perturbations relative to the 1-D initial velocity model in both horizontal and vertical cross-sections.

Consequently, after the tomographic applications, the compatibility of the results with the tectonic and seismological features of the region were evaluated and also compared with the results of the previous studies in the region. The differences between the initial and the final hypocentral parameters were emphasized in various cross-sections.

ÖZET

Doğu Anadolu bölgesi sismik olarak aktif, tektonik ve jeolojik bakımdan ise karmaşık bir yapıya sahiptir. Bölgeye, Doğu Anadolu Projesi (DAP-ETSE) kapsamında 29 adet üç bileşenli geniş bant sismometreden oluşan geçici bir sismik ağ kurulmuştur. Kasım 1999 ve Ağustos 2001 arasındaki dönemde toplanan sismik verilerden yararlanılarak bölgenin kabuk ve üst manto yapısı ile beraber sismisitesi hakkında da ayrıntılı ve güvenilir bulgular elde edilmiştir. Projeden elde edilen sonuçlar, bölgenin tektonik ve jeolojik oluşumunun ve depremselliğinin daha iyi açıklanmasına önemli katkı sağlamıştır.

Bu tez çalışmasında, Doğu Anadolu Projesi'nden elde edilen yerel deprem verileri kullanılarak Doğu Anadolu Platosu ve yakın-çevre bölgelere ait üst kabuk sismik P dalgası hız yapısı üç-boyutlu (3-D) yerel deprem tomografisi (LET) yöntemi ile saptanmaya çalışılmıştır. Çözünürlük açısından bakıldığında, S dalgası okumaları sayısı ve P dalgası okumalarına oranla çok daha az ve okuma hataları daha yüksek olduğundan bu çalışmada kullanılmamıştır. Elde edilen sonuçlar bölgenin tektonik ve sismolojik unsurları ile birlikte yorumlanmaya çalışılmıştır.

LET, sismik olarak aktif bir bölgede ağ içinde kaydedilen yerel depremlere ait seyahat zamanları kullanılarak bölgenin iki veya üç-boyutlu hız yapısının görüntülenmesi işlemidir. Güvenilir sonuçlar elde etmek için kaliteli bir veri setine, güvenilir başlangıç odak koordinatlarına ($-1.0\text{sn} < \text{residüel} < 1.0\text{ sn}$) ve bölgeyi en iyi temsil edecek bir boyutlu hız modeline gereksinim duyulmaktadır.

İlk aşamada, veri derlenmesi ve depremlerin yer bulma işlemi yapılmıştır. 924 adet depremin yer bulma işlemi, önceki çalışmalarda kullanılan düşey yönde bir boyutlu hız modeli ile, rutin bir yer bulma yazılımı olan HYPOCENTER ile gerçekleştirilmiştir.

Yer bulma işleminden sonra bölgenin bir boyutlu hız yapısını belirlemek amacıyla ilk veri setinden kaliteli olarak nitelendirilen depremler seçilmiştir. Kriter olarak azimutal boşlukları ($\text{GAP}) \leq 200^\circ$ ve P dalgası gözlem sayıları ($P) \geq 8$ olan depremler seçilmiştir (Toplam 6978 adet P fazı okuması). Bir boyutlu P dalgası hız modeli eşzamanlı ve yinelemeli ters çözüm yapan VELEST yazılımı ile hesaplanmıştır. Bu yazılım ile bir boyutlu hız modelinin yanı sıra yeni odaksal parametreler ve istasyon düzeltmeleri de hesaplanmıştır. Modelin hesaplanmasında giriş olarak üç farklı hız modeli kullanılmış

ve bu üç modelden 10 yineme ve 2 işlem adımı sonrası elde edilen sonuçlar esas alınarak başlangıç hız modeli oluşturulmuştur.

Tüm modeller bölgenin kabuk yapısına uygun olarak 0-42 km arasında hazırlanmış ancak depremlerin derinlik dağılımından dolayı 25 km'ye kadar daha güvenilir çözümler elde edilmiştir. Son bulunan hız modeli ve istasyon düzeltmeleri kullanılarak depremlerin yer bulma işlemi VELEST yazılımı ile yapılmıştır. Son olarak saptanan bir boyutlu P dalgası hız modelinin çözüm gücü çeşitli şekillerde test edilmiştir. Bu testlerin sonucunda modelin bölgenin yapısını temsil ettiğine karar verilmiştir.

En uygun hız modelinin saptanmasını takiben, son veri seti ile üç boyutlu tomografik ters çözüm yöntemleri uygulanmıştır. Ters çözüm için son veri setinden tekrardan belli kriterlere uygun depremler seçilmiştir ($GAP \leq 180^\circ$ ve $P > 8$). Bu kriterin uygulanması sonucunda tomografik çözümde kullanılan deprem sayısı 504'e inmiştir (toplam 6742 P fazı okuması). Tomografik ters çözüm düğüm noktaları metodunu kullanan SIMULPS14 yazılımı ile gerçekleştirilmiştir. SIMULPS14 yazılımında bir boyutlu başlangıç P dalgası hız modelinden alınan hız değerleri düğüm noktalarına atanmıştır. İstasyon ve deprem dağılımı gözönünde bulundurularak yatay yönde düğüm noktaları aralığı 30km olarak belirlenmiş, düşey yönde ise bir boyutlu başlangıç hız modelinden alınan derinlik değerleri kullanılmıştır. Modelleme başlangıç hız modelinde olduğu gibi 42 km derinliğe kadar yapılmıştır. Uygun kontrol parametreleri ve ters çözüm için kritik olan indirgeme parametresi belirlendikten sonra, dört yineme ve iki işlem adımından oluşan üç boyutlu tomografik ters çözümlere başlanmıştır. Bu işlemlerin sonucunda bölgeye ait üç boyutlu P-hızı dalga modeli ve son odak koordinatları saptanmıştır. Bu aşamalar esnasında varyans (%50) ve residuel (%50) değerlerinde kayda değer azalmalar gözlenmiştir. Daha sonra elde edilen üç boyutlu P dalgası hız modelinin çözümlülük gücü ve sınırlarını saptamak amacı ile sentetik veri kullanılarak çeşitli testler uygulanmıştır. Çözünürlüğü etkileyen kritik parametreler hesaplanmış, mutlak hızlar (V_p) ve başlangıç hız modeline göre % hız değişimleri ile birlikte yatay ve düşey kesitler üzerinde haritalanmıştır.

Tüm tomografik uygulamalardan sonra sonuçların bölgenin tektonik ve sismolojik yapısı ile uyumluluğu irdelenmiş ve önceki çalışmalar ile karşılaştırması yapılmıştır. Elde edilen son deprem koordinatları ile ilk veri seti arasındaki farklar vurgulanmıştır.

1. INTRODUCTION

The primary emphasis of this study is to determine the three-dimensional (3-D) velocity structure of the upper crust for the Eastern Turkey region in a local scale via one-dimensional (1-D) velocity inversions and 3-D tomographic inverse solution techniques, which will also lead to a significant improvement in earthquake location procedure.

Construction of a 3-D velocity model for this medium will considerably contribute to the previously performed studies in the region. As far as the tomographic results are concerned, it is extremely essential to combine overall results with the results of the previous studies in a consistent way. Furthermore, sensible interpretation of the tomographic solutions and consequences along with the geological and tectonic implications is also another crucial factor.

Seismic tomography can be defined as the reconstruction of a field from a knowledge of linear path integrals thorough the field (Clayton 1984). The word 'tomo' comes from the Greek language, which means 'slice'. If we take a slice of a three-dimensional (3-D) object, we obtain a two dimensional (2-D) section. By combining these 2-D slices a 3-D image of the object can be reconstructed. The seismic imaging method was originally called the '3-D inversion' method in the seismological community until the early 1980s.

The first 3-D inversion method (the Aki-Christoffersson- Huseybe method, ACH) was first developed at the NORSAR array center in Norway by Aki, Christoffersson and Huseybe in 1974 using teleseismic earthquakes. The application of this method to local earthquakes for the assessment of the velocity structure of the earth's crust was carried out by Aki et al. (1976,1977) and Aki and Lee (1976). Within a few years, these methods were applied to data from 25 arrays around the world with apertures ranging from 20 to 3000 km, leading to significant 3-D velocity anomalies that can be related to the tectonic implications. Following the landmark paper of Aki et al. (1976), numerous numbers of Ph.D. theses, books and papers have been devoted to the inversion of local travel time data. Hirahara (1977) investigated the upper mantle under Japan delineated the subducting high velocity Pacific plate using this method. Important improvements to the original technique were implemented by Pavlis and Booker (1980) who introduced the separation of parameters technique, allowing the analysis of the large data sets. In the mid-1980s, iterative matrix solvers were introduced by Clayton

and Corner (1983) and Nolet (1985) causing a jump in the number of model parameters. This method is then renamed as 'tomography' that comes from well tested medical applications.

In global scale, application of a similar method to ACH was performed by Dzienowski (1975) and Sengupta (1975). Sengupta and Toksöz (1976) used a small number of deep earthquakes located around the leading edge of several seismic zones in the inversion. In the early 1980s, Dzienowski and Anderson (1984), and Woodhouse and Dzienowski (1984) have managed to construct a seismic image that helped to enhance the believability and the accuracy of the tomographic images.

In local scale, different types of forward solvers (ray tracing schemas) have become a significant part of the LET applications. Thurber (1983) introduced a fast two-point ray tracer with the use of 3-D linear node interpolation. To this regard, Um and Thurber (1987) developed more accurate bending ray tracers and, recently, finite difference and shooting (Runge Kutta Perturbations-RKP) ray tracers were implemented in tomographic studies (Virieux, 1991). More recently, Husen and Kissling (2000) constructed the 3-D image of the subduction zone in north Chile; also Haslinger and Kissling (1999) investigated the 3-D structure around the Gulf of Arta (Greece), Husen et al., (2003) observed the subduction zone structure and the magmatic process beneath Costa Rica by LET.

As far as Eastern Turkey region is concerned, Aktar et al. (2004) used the aftershock sequence of Erzincan Earthquake (13 March 1992, $M_1 = 6.9$) to investigate the 3-D seismic P-wave velocity structure of the Erzincan Basin using the LET method (SIMUL3 code). In addition, 3-D velocity structure of P and S waves for Erzincan Basin by the same method had been the subject of an unpublished PHD thesis of Bülent Kaypak (2002). Both of these studies yielded similar results regarding the velocity anomalies and the main structure of the pull-apart mechanism for Erzincan Basin.

Moreover, LET has been applied extensively to explore the heterogeneous structure of the earth's interior and recently for the investigation of geothermal fields. It has been found very effective to delineate the main features of the velocity and attenuation structure from which important geological conclusions can be drawn.

Considering the tomographic methods, seismic tomography can be primarily classified by the type and distribution of sources and receivers, by whether the whole ray or only part of it is modeled, by the type of data used, by the type of error minimization (generally least-squares), by the *a priori* constraints and by the type of inversion. Major methods are described below:

Classification in terms of source;

- a) Earthquake tomography: Natural sources are used in this case. Hypocenter-velocity structure coupling becomes the important part of the problem due to the unknown hypocentral parameters (latitude, longitude and depth) and origin times of the earthquakes used. This restriction requires relocation of earthquakes in the inversion procedure. The receivers are the stations in earthquake tomography.
- b) Controlled source tomography: Man-made events such as shots or blasts are used in controlled source tomography. In this case the exact location and the origin time of the source are known, which is the opposite case to earthquake tomography. Due to known source parameters, hypocenter-velocity structure coupling does not become a part of the problem.

Classification in terms of source receiver-geometry;

- a) Local earthquake tomography (LET): In LET applications, the structure of upper crust is resolved in a local scale. Sources and receivers lie within the same model space (which is the case in this study) where the observed phases are mostly the direct arrivals (Pg, Sg). The events must occur in the model volume and be measured by a grossly homogeneous network of seismographs approximately spanning the target volume.

Useful introductions to the field of Local Earthquake Tomography (LET) can be found in Kissling (1988) and Thurber (1993). LET comprises the inversion of travel times, recorded locally, for Vp and Vs velocities or Vp/Vs ratios.

Model parameters are perturbed to minimize the difference between observed and calculated travel times (residuals) in a least square sense. Synthetic travel times are calculated using mostly ray tracing methods. A further discussion of LET theory will be given in Chapter 5.

b) **Teleseismic Tomography:** In contrast to local earthquake tomography, long-period seismic signals ($T > 30$ seconds) recorded at a densely spaced seismic array are used to model the velocity structure of whole earth in a spherical scale. Data is provided by international seismic network around the globe. The basic idea is that in the absence of heterogeneity the incident wavefronts should have a simple plane-wave velocity across the array. One of the major drawbacks of this method is the lack of high resolution in terms of the tomographic imaging.

Velocity and attenuation tomography are also used to derive the main properties of the crust relevant to the tomographic studies.

Another widely used tomography methods are referred as the series expansion methods. These methods start by considering the object or area of interest to be comprised of boxes or pixels. Energy is considered to propagate through the various pixels to provide a sum or projection of the pixel values. The pixel values are now correlated to the sum. This is often related to solving large linear equations. A stable but approximate solution, as discussed above is known as backprojection. In the matrix formulation, backprojection corresponds to using the transpose of matrix instead of the inverse. Two other more accurate but iterative methods are known as ART (Algebraic Reconstruction Technique) and SIRT (Simultaneous Iterative Reconstruction Technique). These techniques require high-capacity computers.

Following the general overview and the major applications seismic tomography, the tectonic setting of Eastern Turkey was briefly given followed by the previous studies for the region in section 2.

Station distribution and the equipment specifications of the temporary Eastern Turkey Seismic Experiment (ETSE) network, seismic data compilation and initial earthquake location procedure via initial one-dimensional (1-D) P wave velocity model are explained in section 3.

In section 4, derivation of the 1-D minimum P wave velocity model (which serves as an initial velocity model for the tomographic inversion) was presented in quite detail along with the theory and calculation steps. Depending on a certain criteria, proper data selection was made for the 1-D simultaneous velocity inversion via VELEST algorithm with several trial velocity models (with certain number of iterations) and the final event

locations are shown. Systematic and random event shifting tests were performed in order to test the stability of the minimum 1-D velocity model.

In section 5, derivation of the 3-D P wave velocity model was depicted extensively along with the basic LET method and its implications. Tomographic inversions via SIMULPS14 algorithm were performed with the appropriate model parametrization (node-grid spacing) and the control parameters (residual weighting, damping factor etc.). Beforehand, two distinct resolution tests using synthetic travel time data were also performed in order to assess the solution quality and the resolving power of the resulting 3-D P wave velocity model. Basic resolution parameters, results of the synthetic tests and the actual tomographic inversion results were mapped in different cross-sections and views together with the updated hypocenter locations.

Conclusions that are based on the overall tomographic images results were briefly explained and interpreted from a tectonic point of view in section 6.

2. TECTONIC STRUCTURE OF EASTERN TURKEY AND PREVIOUS SEISMIC STUDIES

The tectonic structure of the region is quite complex. Eastern Turkey is an extremely deformed high plateau, located behind the continent-continent collision zone of the Arabian and Eurasian plates, which is a part of the Alpine-Himalayan mountain belt. In tectonic approach, it has been well documented that Anatolian Plateau can be described as the convergence of the Anatolian, Arabian and Eurasian Plates that form the major tectonic boundaries in the region such as the East Anatolian Fault Zone (EAFZ), the North Anatolian Fault Zone (NAFZ) and the Bitlis thrust belt (Figure 2.1).

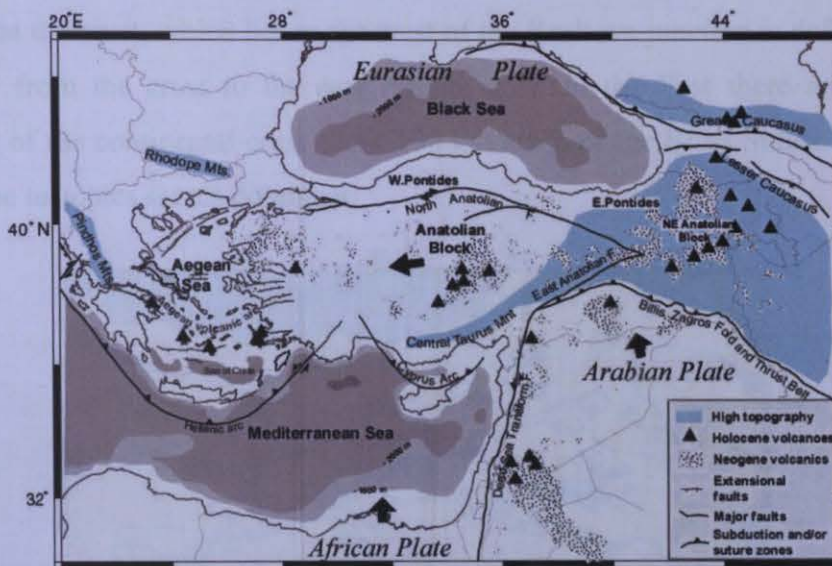


Figure 2.1. Map showing the major tectonic structure of Eastern Turkey and surrounding regions (Gök, R. 2000 and modified after Barka and Reilinger, 1997).

Arabian plate collides with the Eurasian plate to form the Turkish-Iranian Plateau that causes movement along the North and East Anatolian fault zones. The East Anatolian Plateau with an average of 2 km elevation can be thought of as a younger version of the Tibetan Plateau (Şengör and Kidd, 1979; Dewey et al., 1986; Barazangi, 1989). The Arabian-Eurasian collision is associated with high volcanism in Eastern Anatolia, starting in late Miocene (Keskin et al., 1998; Yilmaz, 1990). This volcanism is originated from the lower portion of the lithospheric mantle (Pearce et al., 1990)

The motion of Arabian plate towards north relative to Eurasia leads to lateral movement of the Anatolian block to the west. Right-lateral strike-slip movements along the NAFZ

(Şengör, 1979; Dewey and Şengör, 1979; McClusky et al., 2000) and left lateral strike-slip movement along the EAFZ (Mckenzie, 1972; Jackson and Mckenzie, 1988) indicate this tectonic escape. Farther north, the Lesser and the Greater Caucasus regions which are thought to partially accommodate the Arabian plate northward motion (Philip et al., 2001) are undergoing thrust and strike slip deformation. The NAFZ and EAFZ have been active since the Miocene (Barka and Kadinsky-Cade, 1988) and contain large pull apart basins such as Karlioiva junction. Karlioiva Basin is located at the junction of these two major fault systems. To the east of the Karlioiva junction, the East Anatolian Plateau appears an internal deformation zone characterized by NW and NE trending active strike slip faults. Furthermore, GPS measurements from Reilinger et al. (1997) indicate that the crust, which lies to the west of the Karlioiva junction is deforming very differently from the crust to the east (Figure 2.2). In the East there appears to be shortening of the continental crust about 150 km north of the Bitlis Suture while in the west escape tectonics seems dominant.

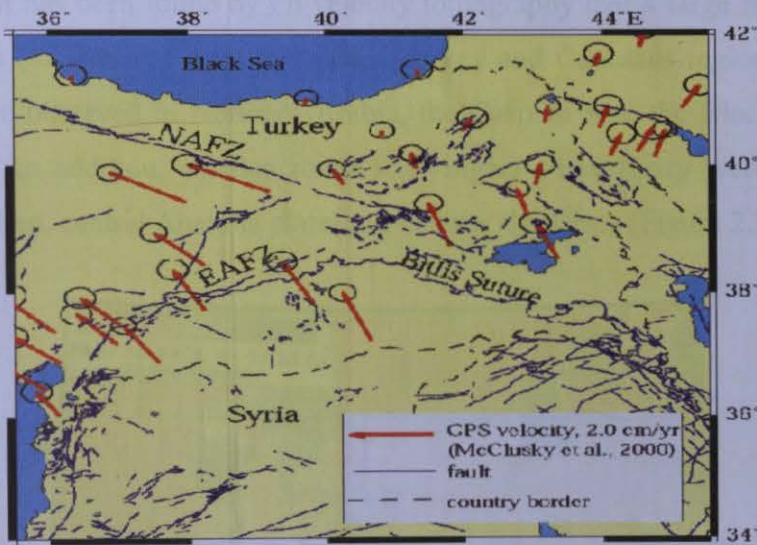


Figure 2.2. GPS velocity vectors for Eastern Turkey (Reilinger et al, 1997).

Eastern Turkey Seismic Experiment (ETSE) was carried out in order to address the crucial questions relevant to the tectonic evolution of the Anatolian Plateau including whether the northward movement of the Arabian plate is governed by lithospheric thickening (Şengör and Kidd, 1979; Dewey et al., 1986), continental escape (Jackson and Mckenzie, 1988), lithospheric delamination (Pearce et al., 1990), continental subduction (Rotstein and Kafka, 1982) or a combination of these processes.

2.1 PREVIOUS SEISMIC STUDIES IN EASTERN TURKEY

Recently, crustal structure and the tectonic evolution of Eastern Turkey region was extensively studied in the context of Eastern Turkey Seismic Experiment (ETSE) from late 1999 to August 2001. Collision of the Arabian and Eurasian plates has been occurring along EAFZ (East Anatolian Fault Zone) and the Bitlis Suture, which made Eastern Turkey an ideal platform for scientific research.

Considering the results of this project, it was found that there was a complete lack of subcrustal earthquakes (Turkelli et.al, 2003) and observed focal mechanisms suggested that most of the collision was taken up by strike-slip faulting (Örgülü and Aktar, 2003). An average crustal thickness of 45 km and an average crustal shear velocity of 3.7 km/s were derived for the entire eastern Anatolian Plateau and 2km topography is dynamically supported because the plateau appears to be isostatically under-compensated (Zor et.al, 2003).

Furthermore, it has been found by Pn velocity tomography that a large zone of low Pn velocity zones (<8 km/sec) exist in Eastern Turkey and Caucasus region and high Pn velocities were observed in Northern Arabia, the Caspian Sea, the Black Sea (Ali Al Lazki, 2003). In addition, smaller zones with higher Pn velocity were observed in northwestern Iran, central Anatolia plate, and Greater Caucasus (Figure 2.3).

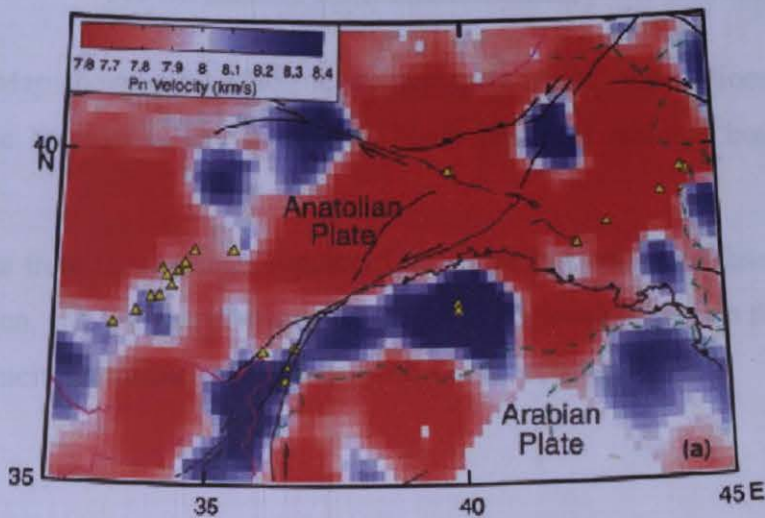


Figure 2.3. Map showing the tomographic image of Pn velocity. Blank lines indicate the major faults. Pink lines show the coastlines and green dashed lines represent the national boundaries. (Al Lazki, 2003)

Comparably, Sn wave propagation study by Gok et.al, (2003) also indicates blocked Sn phases due to high attenuation beneath the Anatolian Plateau and the Caucasus region (Figure 2.4). Bitlis suture zone appeared to be sharp transition both from efficient Sn to no Sn propagation and from low to high Pn velocity zones. Moreover, it was suggested that zones of Sn blockage might be caused by partial melt within the uppermost mantle or irregularities in the upper mantle Sn wave-guide (scattering attenuation).

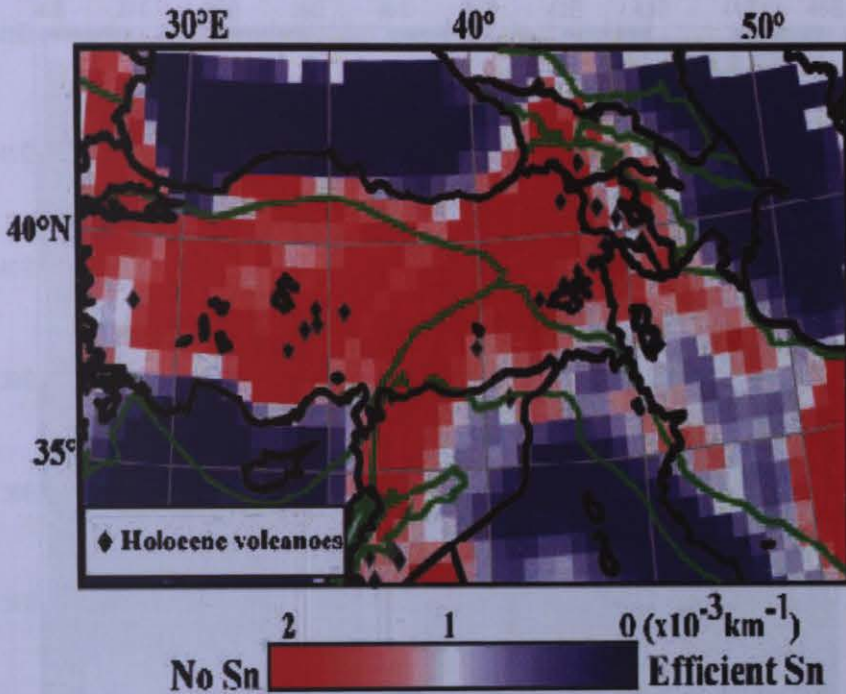


Figure 2.4. Map showing Sn efficiency tomography results. Green lines represent the major tectonic boundaries and coastlines; blank lines are national boundaries (Gok et.al., 2003).

Overall results from these studies suggested that there is a complete absence of mantle lid in the region, and asthenospheric material is directly located beneath the crust and in general, seismicity terminates after 25 km with a few exceptions.

3. STATION NETWORK AND DATA COMPILATION

Eastern Turkey Seismic Experiment (ETSE) was conducted from late October 1999 to August 2001 across the East Anatolian Plateau and the northernmost Arabian plate in order to obtain accurate location of both micro-earthquakes and subcrustal events. The ETSE seismic network was a PASSCAL array that consisted of 29 broadband stations (Figure 3.1).

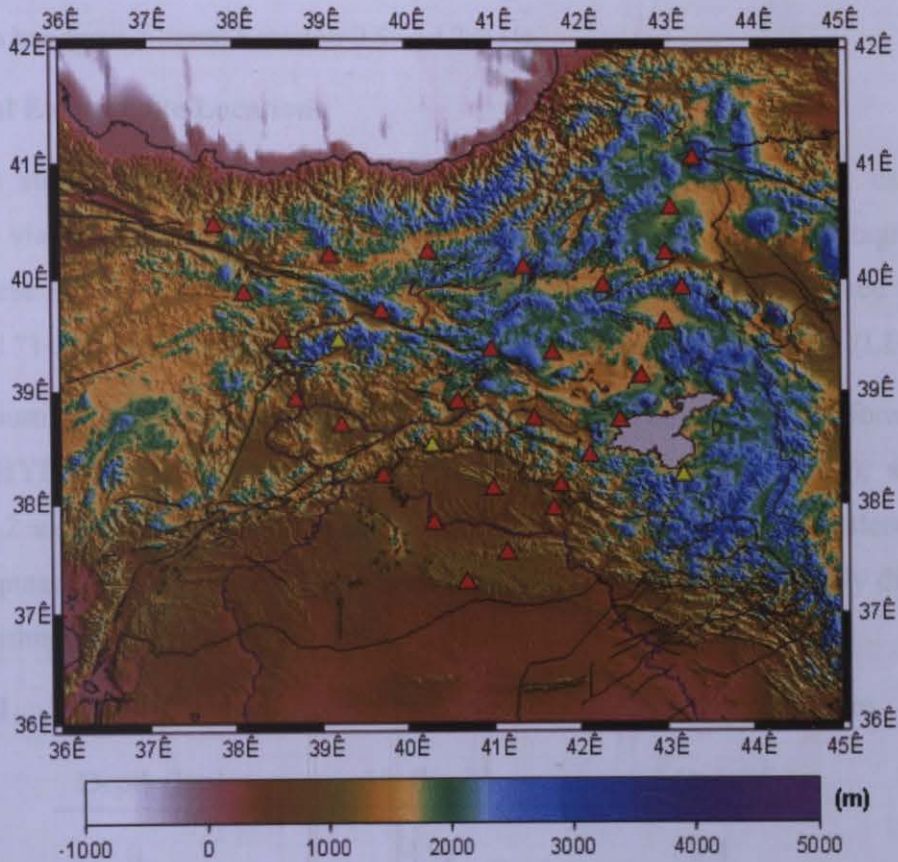


Figure 3.1. Station geometry of the ETSE seismic network. Red triangles denote the ETSE stations and yellow triangles denote the local permanent short period stations. Major faults are indicated with black lines.

The eastern and the western lines of the array formed a “V” shape in terms of geometry. The average station spacing was 50 km for the western line and 30 km for the eastern line.

All the broadband stations were equipped with a STS-2 seismometer, a REFTEK 72A recorder with a 4 GB field disk except the station EZRM where a GURALP-3T was used. 24 bit continuous data at 40 sps (sample per second) were recorded by ETSE

seismic network. In addition; three vertical component short period stations (VANT, BNGT and ERZT) of Kandilli Observatory and Earthquake Research Institute (KOERI) were used in order to increase the station and ray coverage.

Event triggering was performed by an automatic network-triggering algorithm using the STA (short term average) and LTA (long term average) and their ratio, STA/LTA parameters. Proper values of 10 seconds, 50 seconds and 1.70 for STA, LTA and STA/LTA were calculated respectively by taking into account the noise level. The data were also bandpass filtered between 0.5 and 2.0 Hz.

3.1 Initial Earthquake Locations

The first step of the tomographic applications is to obtain the initial earthquake locations via a priori one-dimensional (1-D) velocity model. In the latter stages of this study, these initial locations and the 1-D starting velocity model will be used to derive the initial “1-D minimum velocity model” for local earthquake tomography (LET)

A total number of 944 earthquake locations in Eastern Turkey were performed by a routine HYPOCENTER location algorithm (Lienert and Haskov, 1995), shown in Figure 3.2 along with depth distribution. The 1-D velocity model for Eastern Turkey was computed from a grid search approach for accurately located and evenly distributed events within the ETSE network (Table 3.1, Türkelli et al., 2003).

Table 3.1. Initial 1-D velocity model used in earthquake location procedure.

Depth (km)	Vp (km/s)	ρ (gr/cm ³)
0	4.93	2.4
2	6.30	2.6
42	7.69	3.0

The crustal model were tested and calibrated by a 12-ton controlled source explosion that was conducted in Eastern Turkey (Gurbuz et al., 2003).

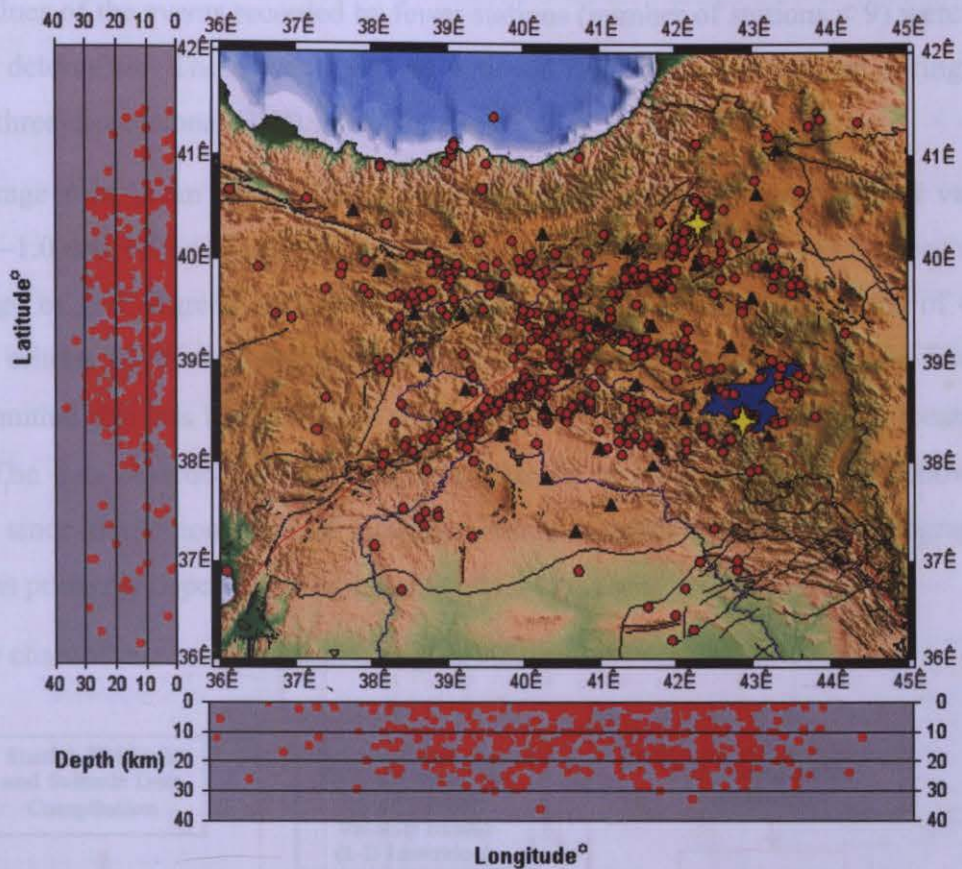


Figure 3.2. Initial earthquake locations and depth distribution along with latitude and longitude depth cross-sections. Yellow triangles represent the stations and red circles represent the events. Blue stars denote two moderate size earthquakes.

During the experiment two moderate size events occurred near Şenkaya (3 December 1999, $M_w = 5.5$) and near Lake Van (15 November 2000, $M_w = 5.3$) that are also shown in Figure 3.2 with blue triangles.

It has been found that for near surface events, the ETSE network is able to locate events within 2-3 km of the true epicenter even when not using an optimal velocity model and the hypocentral errors cannot exceed 5 km for well located events (Türkelli et al., 2003). For the well-located events inside the network, the horizontal and vertical errors are between 3-5 km and 5-9 km respectively. During the initial location procedure, only two events with depth values exceeding 30 km were observed. As shown in Figure 3.2, majority of the event depths are distributed in the 0-25 km range.

Depth values of the events recorded by fewer stations (number of stations < 9) were not precisely determined. These events will be removed from the initial data set during the 1-D and three-dimensional (3-D) inversion steps.

The average root mean square (RMS) error is of order of 0.5 seconds and varies between -1.0 and $+1.0$ seconds. Azimuthal gap varies between 41 and 343 degrees with an average of 165 degrees. Azimuthal gap is an essential parameter in terms of data selection criteria for the 1-D and the 3-D inversion in tomographic applications. Events with azimuthal gap less than 180° are considered to be high-quality and well locatable events. The data selection criteria will be explained in more detail in the following sections since derivation of 1-D minimum velocity models and 3-D tomographic inversions primarily depend on a high-quality data set.

The flow chart of this study is given in Figure 3.3.

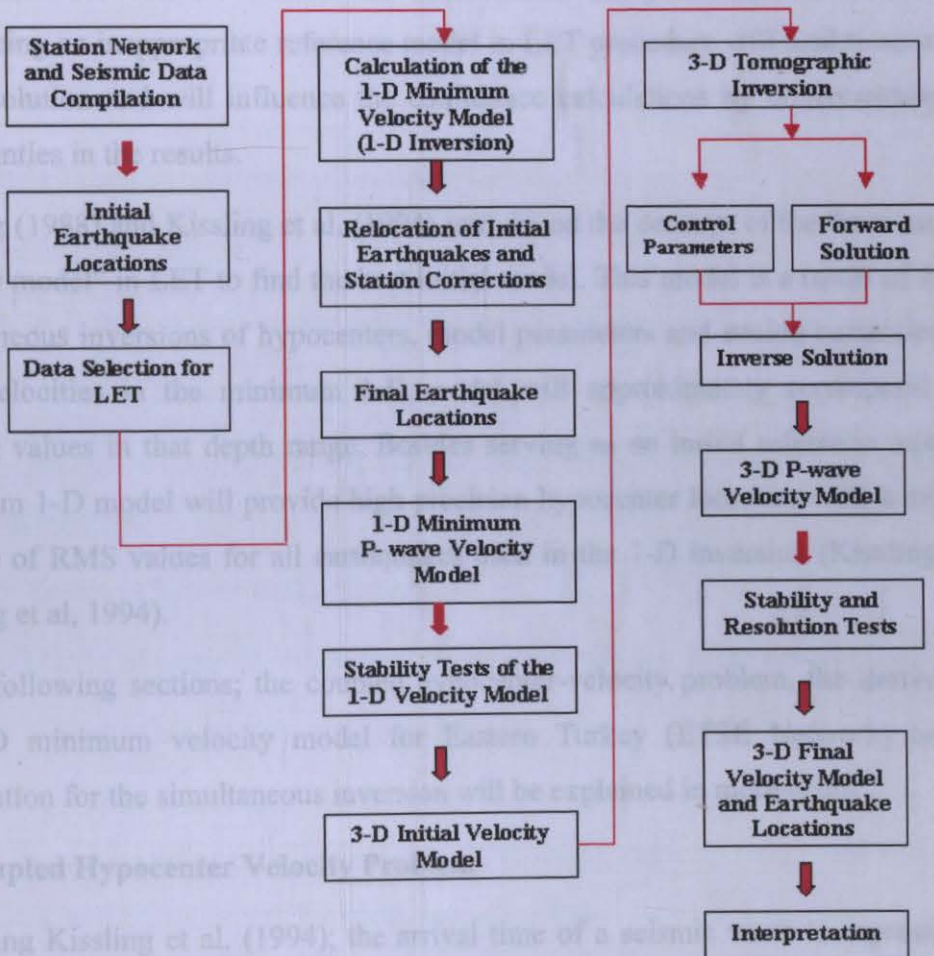


Figure 3.3. Flow chart and the calculation steps of the study

4. DERIVATION OF THE 1-D MINIMUM VELOCITY MODEL FOR LOCAL EARTHQUAKE TOMOGRAPHY (LET)

Three-dimensional (3-D) inverse problems such as local earthquake tomography (LET) are formulated as linear approximations to nonlinear functions. The major goal of LET is to improve the estimates of the model parameters by perturbing them in order to minimize the weighted root-mean-square (RMS). In most LET applications, solutions are obtained with respect to a reference earth model (e.g., Aki and Lee, 1976). The solution quality of the tomographic images is strongly dependent on the initial reference models and hypocentral locations (Kissling et al., 1994).

Computation of one-dimensional (1-D) velocity models generally starts with introducing a simple smooth model that represents some weighted average of the observations. Then this model is modified to some extent until a sufficient degree of coincidence between the bulk of the observations and predicted values is reached. Introducing an inappropriate reference model in LET procedure will lead to severe bias in the solution and will influence the confidence calculations by underestimating the uncertainties in the results.

Kissling (1988) and Kissling et al. (1994) introduced the concept of the “minimum 1-D velocity model” in LET to find the best initial model. This model is a result of series of simultaneous inversions of hypocenters, model parameters and station corrections. The layer velocities in the minimum 1-D model will approximately correspond to the average values in that depth range. Besides serving as an initial reference model, the minimum 1-D model will provide high precision hypocenter locations with a minimum average of RMS values for all earthquakes used in the 1-D inversion (Kissling, 1988, Kissling et al, 1994).

In the following sections; the coupled hypocenter-velocity problem, the derivation of the 1-D minimum velocity model for Eastern Turkey (ETSE Network) and data compilation for the simultaneous inversion will be explained in more detail.

4.1 Coupled Hypocenter Velocity Problem

Following Kissling et al. (1994); the arrival time of a seismic wave is expressed as a nonlinear function of the station coordinates (s),

the hypocentral parameters (h , including origin time and geographic coordinates), and the velocity field (m):

$$\mathbf{t}_{\text{obs}} = \mathbf{f}(\mathbf{s}, \mathbf{h}, \mathbf{m}). \quad (4.1)$$

Hypocenter parameters and velocity field are not known in this case. Arrival times and the station coordinates are the only measurable quantities in equation (4.1). Using a priori velocity model rays are traced from a trial source location to the receivers and the theoretical arrival times (t_{calc}) are calculated. The travel time residual (t_{res}) can be expanded as functions of the differences between the estimated and the true hypocentral and velocity parameters. The dependence of the observed arrival times on all parameters should be precisely known in order to calculate the suitable adjustments (corrections). This dependence on the origin time is strongly nonlinear (e.g., Thurber, 1985). We obtain the linear relationship between t_{res} and adjustments to the hypocentral (Δh_k) and velocity (Δm_i) parameters in the following equation:

$$t_{\text{res}} = t_{\text{obs}} - t_{\text{calc}} = \sum_{k=1}^4 \frac{\partial f}{\partial f_k} \Delta h_k + \sum_{i=1}^n \frac{\partial f}{\partial m_i} \Delta m_i + e. \quad (4.2)$$

Equation (4.2) can be written in matrix notation as:

$$\mathbf{t} = \mathbf{Hh} + \mathbf{Mm} + \mathbf{e} = \mathbf{Ad} + \mathbf{e} \quad (4.3)$$

Equation (4.3) is so called the coupled hypocenter-velocity model problem where:

- \mathbf{t} : Vector of travel time residuals,
- \mathbf{H} : Matrix of partial derivatives of travel time with respect to hypocentral parameters,
- \mathbf{h} : Vector of hypocentral adjustments,
- \mathbf{M} : Matrix of partial derivatives of travel time with respect to model parameters,
- \mathbf{m} : Vector of model parameter adjustments,
- \mathbf{e} : Vector of travel time errors, including errors in measuring t_{res} , errors in t_{calc} due to errors in station coordinates, use of the wrong velocity model and hypocentral coordinates, and errors caused by linear approximation.

A : Matrix of all partial derivatives

d : Vector of hypocentral and model parameter adjustments.

Ignoring the effect of hypocenter-velocity structure coupling, which is the term $\mathbf{H}\Delta\mathbf{h}$ in equation (4.3) will introduce systematic errors into the estimated hypocenter during the location process (Thurber, 1992; Eberhart-Philips and Michael, 1993). Similarly, ignoring the effect of $\mathbf{M}\Delta\mathbf{m}$ might result in biased velocity parameters (Michael, 1988).

4.2 Concept Of The Minimum 1-D Velocity Model

Determination the appropriate minimum 1-D velocity model ideally starts with the construction of a model that itself represents the least squares solution to equation 4.3 (Kissling et al., 1994). Use of the minimum 1-D model also allows us to test for the significance of the 3-D model in terms of the variance reduction ratio in the final solution. Computation of the minimum 1-D velocity model is a trial and error process that begins with the collection and selection of a priori information about the subsurface structure. Several parameters in the control files need to be varied and carefully evaluated during the inversion process. The results of this inversion strongly depend on the proper data selection process (number of well locatable events and their distribution, minimum number of observations per event, azimuthal gap, station geometry and epicentral distance to next station).

In this study, calculation of the 1-D minimum velocity model is performed by a Fortran code VELEST (Kissling et al., 1994, Kissling et al., 1995) that simultaneously computes the epicenters and the station corrections in an iterative process. VELEST code requires an initial velocity model, travel times for each earthquake-station pair, station coordinates and delay times (to calculate the station corrections).

To account for lateral variations in the shallow subsurface, station corrections are included in the inversion. The initial velocity model should consist of constant horizontal layers where the velocity values increase with depth. This initial reference model should thus be constructed using similar distribution of sources and the receivers as the data set being analyzed for 3-D structure (Kissling et al, 1994). Velocity model calculation procedures do not guarantee convergence to a best solution. Specific characteristics of the data set and the velocity structure have to be imposed accurately in

the calculation process (Kissling, 1988). The steps of 1-D velocity model calculation will be given extensively in the following section.

4.3 Calculation Steps of the 1-D Initial Velocity Model

- 1) To begin with, all a priori information regarding the area under study should be obtained (layer velocities and thicknesses) as previously mentioned above (section 4.2). This information may include seismic reflection and refraction studies or a general crustal model. Then, the media is defined by several layers of increasing velocity with depth. Layer thickness in the upper crust should be about 2-3km and in the lower crust about 4-5 km. VELEST requires a reliable reference station, preferably located in the center of the network and should also be not situated in an area with unknown or complex surface geology. To probe the dependence of the solution on the initial model one should try at least three different initial velocity models for any model geometry: one with extremely low crustal velocities, one with extremely high and one with intermediate crustal velocities (*VELEST users guide*). After this step this model is called a “piori” 1-D velocity model.
- 2) The best events with high quality P arrivals in the data set (approximately 500 events) should be selected to cover the entire area under study. These events are relocated by VELEST using the appropriate damping values for each model parameter. This procedure is repeated several times with updated (new) velocities, station delays, and with new hypocenter locations. In addition, adjacent layers with similar velocities can be combined during the inversion.

The procedure in this second step should also be applied for the combined layers. In most cases, low velocity layers should be avoided due to the instabilities they introduce to the problem.

Kissling et al., (1994) suggests that shot or blast data (controlled-sources) should not used in the inversion. Rather such data can be used to test the performance of the final minimum 1-D model. We can proceed to the next step if the following criteria are reached:

- (a) when the earthquake locations, station delays and velocity values do not vary considerably in subsequent runs,

- (b) when RMS values of all events indicate a considerable reduction,
- (c) when the calculated 1-D velocity model and the station corrections make geological sense.

If all these requirements are fulfilled the resulting model can be called the “updated a priori 1-D model with corresponding station residuals” (Kissling et al., 1994).

- 3) Following the second step; all events are relocated using the updated velocity model with a routine location problem such as HYPO71 (Lee and Lahr, 1975), HYPOCENTER (Lienert and Haskov, 1995) or with VELEST in the single event mode. Again a new set of well locatable events (around 500) will be selected from the data set.
- 4) In this part, the step 2 is repeated with the new data set obtained from step 3 with the relevant damping parameters. This step is executed in order to find the best velocity model that minimizes the overall location errors for the fixed geometry. This step is repeated until the satisfaction requirements in step 2 are reached.

4.4 Calculation Of 1-D Minimum Velocity Model For Eastern Turkey

A total number of 523 well locatable events with an azimuthal gap less than 200° and with at least ϕ P-phase observations were selected from the initially located data set (total number of 944 events) for the one dimensional (1-D) velocity inversion via VELEST algorithm. The selected events (yellow circles) and their depth distribution (latitude and longitude depth cross-sections) are shown in Figure 4.1 along with the initial earthquake locations based on a certain data selection criteria mentioned above.

As seen in Figure 4.1, majority of the selected events are located within the ETSE network with a few exceptions. In latter stages; during the three dimensional (3-D) tomographic inversion, events that are located outside the ETSE network will be removed in order to obtain more accurate results.

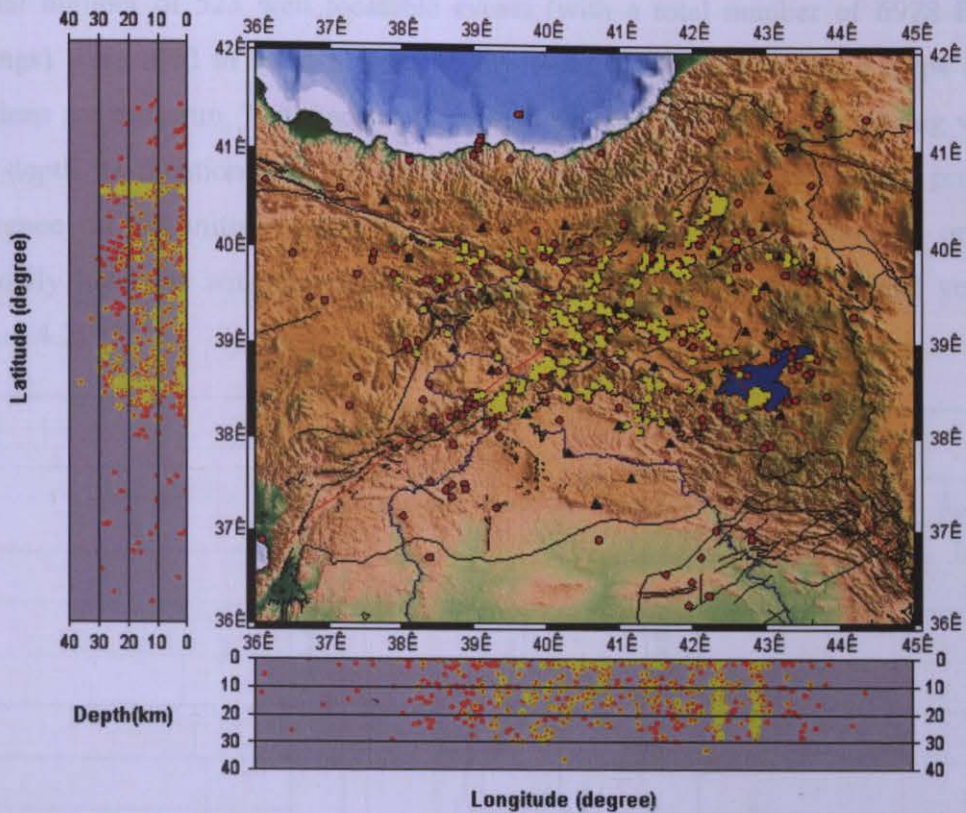


Figure 4.1. Events used for the 1-D velocity inversion (yellow circles) along with their depth distribution (open yellow circles in both depth cross sections) and the initial locations (red circles).

Azimuthal gap values vary between 41° and 200° with an average of 131° in the selected data set for the 1-D inversion. The average root mean square (RMS) value for the selected data set is in order of 0.5 seconds and whole RMS values vary between -1.0 and 1.0 seconds. Event selection criteria is not primarily based on the RMS values, since we will be seeking a significant reduction in this parameter after the 1-D velocity inversion in order to make a comparison between the initial and the minimum 1-D velocity models for a sensible interpretation.

To begin with; since there has not been a seismic reflection study performed in the region before, we used the 1-D velocity model (which is also used in the initial earthquake location procedure) obtained from the grid search approach (Türkelli et al., 2003) as a starting point. This velocity model is perturbed to a certain extent by a trail-error process in order to reach the best fitting 1-D minimum velocity model for the region.

A total number of 523 well locatable events (with a total number of 6978 P phase readings) were used in the 1-D velocity inversion with two calculation steps and ten iterations for each run. The media was defined by several layers of increasing velocity with depth as mentioned in the previous section (calculation steps). To probe the difference on the initial model we used three different velocity models: one with extremely low, one with extremely high and one with intermediate crustal velocities (Figure 4.2).

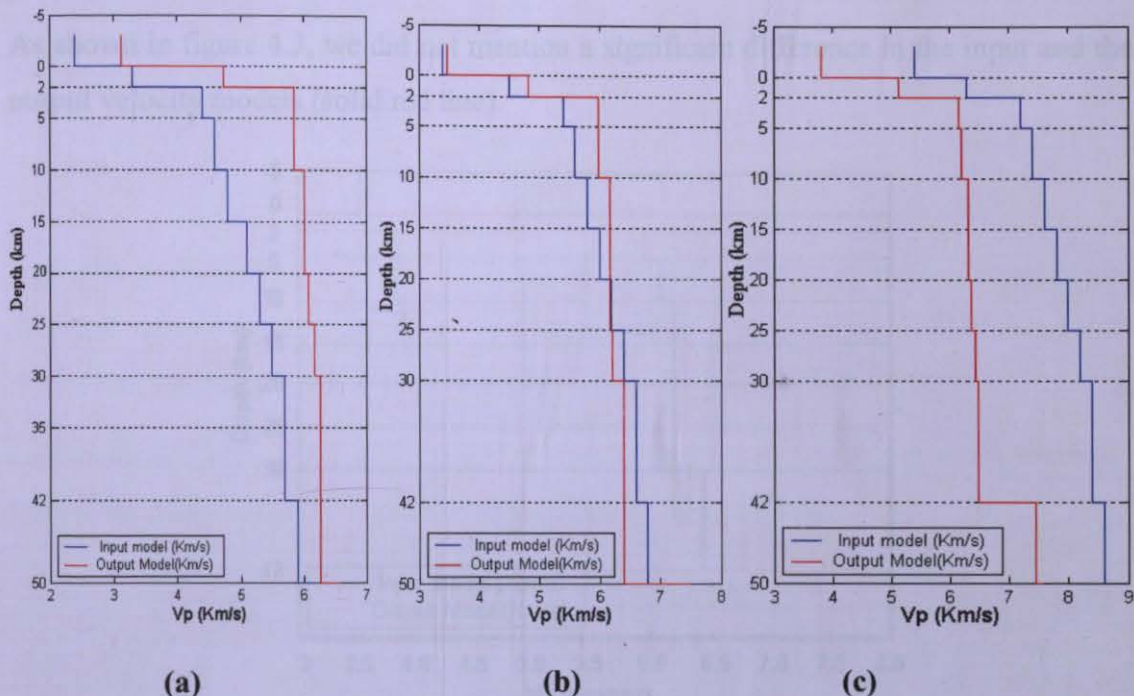


Figure 4.2. Inversion results for three trial velocity models: (a) with low velocities, (b) with intermediate velocities, and (c) with high velocities. Red line denotes the output and the blue line denotes the input velocity model.

Depth range of each model varies between -2 and 42 km due to the crustal structure of the region and the station elevations. Updated results from each run (hypocenter locations, station delays and velocities) were used as the inputs for the following runs along with the appropriate control parameters. Adjacent layers with similar velocities were combined during the inversion process. As seen in Figure 4.2, we observed a considerable convergence in velocity values for each of the three trial velocity models in 0 - 25 km depth range. This result suggests that 0 - 25 km depth range is well resolved by the data. On the contrary, these trial models with higher, lower and intermediate

velocities are not accurately constrained below 25 km due to the lack of seismicity in this depth range.

A new velocity model depending on the initial runs was constructed and the resulting velocity values were kept in between the initial velocity intervals of the three trial models. In Figure 4.3, the overall output model velocity model obtained from the three previous runs (solid blue line) is again inverted with the updated inversion parameters and the relevant control parameters.

As shown in figure 4.3, we did not mention a significant difference in the input and the output velocity models (solid red line).

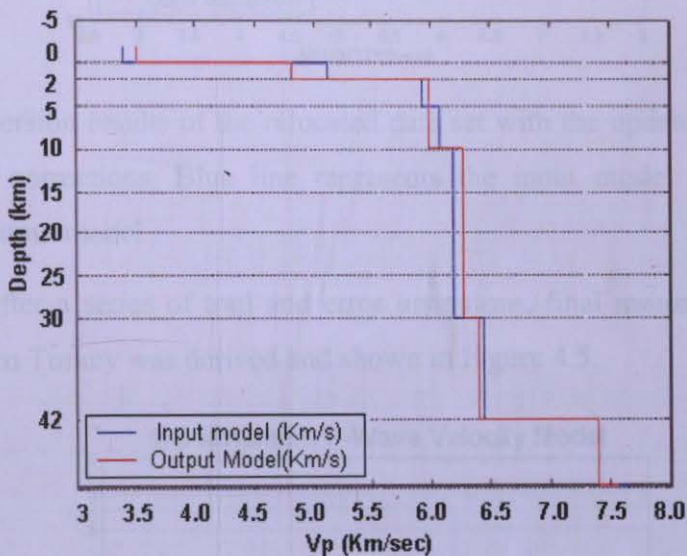


Figure 4.3. Inversion results for the resulting velocity model (blue line) from the previous inversion with three different trial velocity models. Red line represents the output velocity model.

Two velocity models seemed to be well converged and consistent within certain velocity values in 0-25 km depth range. We call this resulting velocity model “updated a priori 1-D velocity model” with the corresponding station residuals.

Furthermore, another velocity inversion was performed using the initial data set along with the updated station residuals from the previous inversions. All events were relocated by VELEST in “single event” mode with the updated P wave velocity model (Figure 4.4). The final inversion did not also show a significant difference in subsequent runs and the output model looked to be consistent with the given updated input velocity

model. Moreover, the RMS values and the data variance have considerably decreased as a result of the several iterations in the velocity inversion.

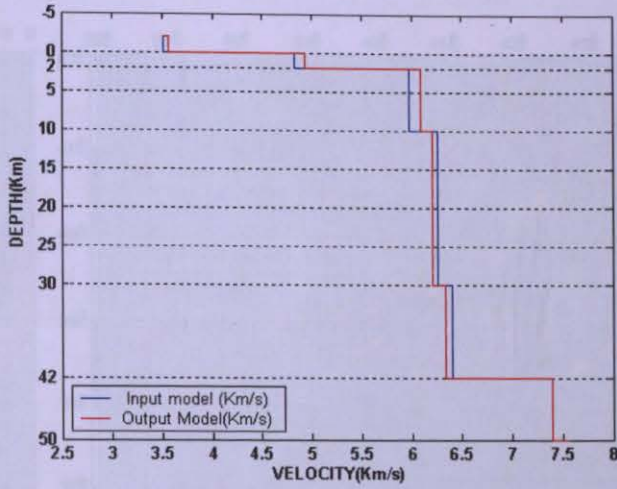


Figure 4.4. Inversion results of the relocated data set with the updated velocity model and the station corrections. Blue line represents the input model and the red line represents the output model.

Consequently, after a series of trial and error inversions, final minimum 1-D velocity model for Eastern Turkey was derived and shown in Figure 4.5.

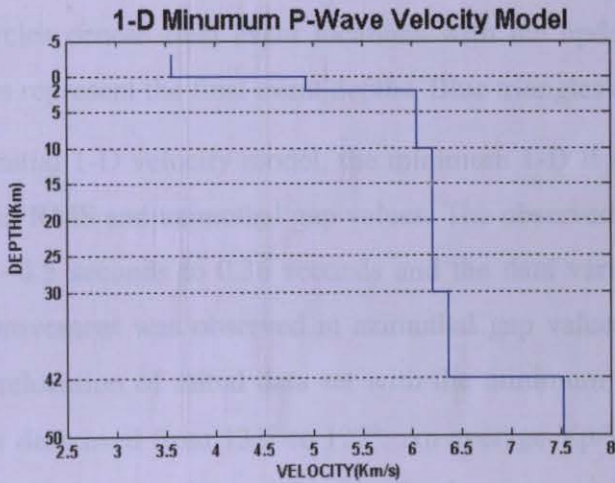


Figure 4.5. 1-D Minimum P wave velocity model for Eastern Turkey obtained from the previous velocity inversions (blue line).

The final event locations are shown in Figure 4.6 along with the initial event locations. Reduced hypocenter scattering is apparent for the aftershocks of Senkaya and Gevas mainshocks after the relocation via 1-D minimum velocity model. Hypocenter depths

are also clustered and mostly moved upwards with respect to their initial positions. Average horizontal hypocenter displacement is in order of $\sim 3\text{km}$.

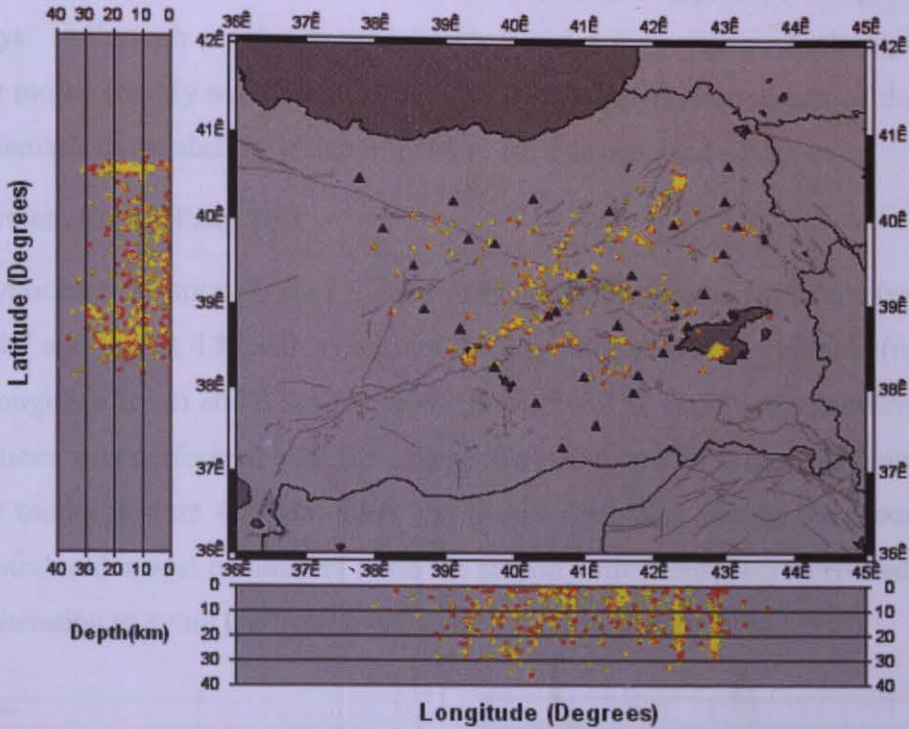


Figure 4.6. The initial and the final earthquake locations. Red circles denote the initial and the yellow circles denote final event locations with the updated velocity model. Open yellow circles represent the final event depths. Blue triangles denote the stations.

Compared to the initial 1-D velocity model, the minimum 1-D P wave velocity model led to a reduction in RMS and azimuthal gap values. The observed average RMS value has reduced from ~ 0.5 seconds to 0.36 seconds and the data variance has reduced to 0.22. Another improvement was observed in azimuthal gap values. After the velocity inversion and the relocation of initial data set with the minimum 1-D velocity model, average gap values decreased from 131° to 122° . An average V_p/V_s value of 1.80 was used to constrain the S-phases and the earthquake depths more accurately.

4.5 Stability Tests for the 1-D P-Wave Velocity Model

In this section, the stability of the 1-D minimum P wave velocity model is tested to assess the model quality. The velocity inversion was started with event locations, which were systematically and randomly perturbed in their three spatial coordinates.

Every hypocenter is shifted 7 to 8 kilometers in each direction (x,y,z) with the actual value obtained from a random distribution. Shallow events that would be moved above the surface were shifted downwards in “z” direction. Shifting process was performed in two ways: 1) through a velocity model with low damping values, 2) through a fixed velocity model (highly overdamped velocity values). The further results of the random and systematic event shifting tests are given in the following sub-sections.

4.5.1 Systematic Shifting Test

Final hypocenter locations were systematically shifted in three coordinates (red dots in Figure 4.7 and Figure 4.8) with a constant shifting value of 8 km in latitude (north), 7.8 km in longitude (east) and 8 km for depth (upwards). The simultaneous inversion with 15 iterations was performed both for a damped velocity model (Figure 4.7) and a fixed velocity model (Figure 4.8) that allow the hypocenters float during the process. Both hypocentral and model parameters (with the station corrections) were inverted in every second iteration to avoid the hypocenter-velocity structure coupling.

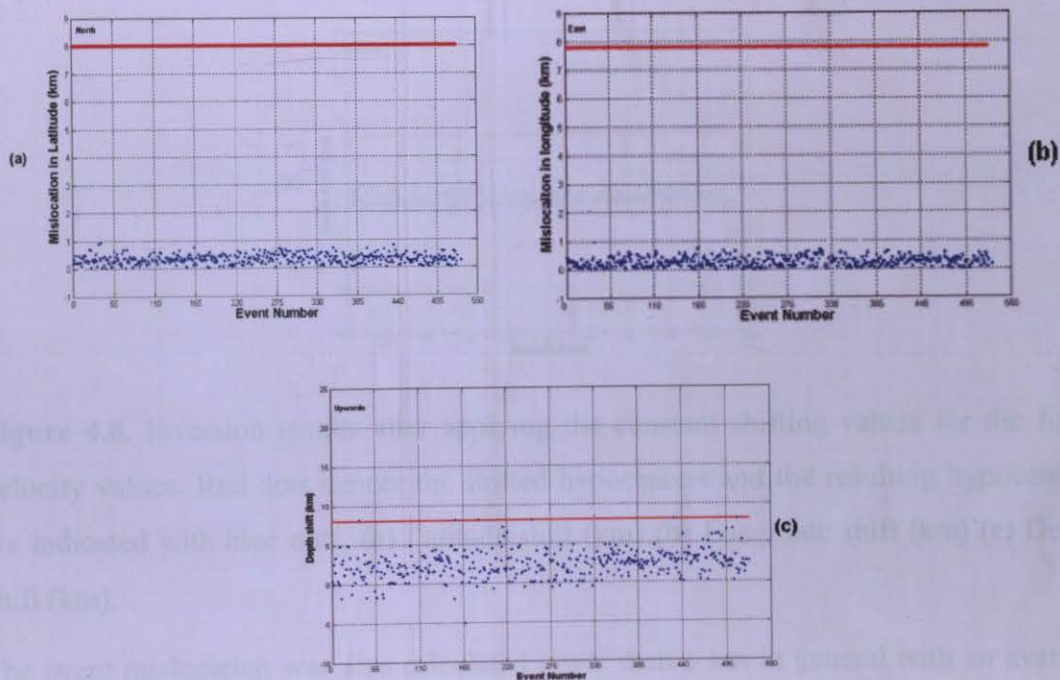


Figure 4.7. Inversion results after applying the constant shifting values for the underdamped velocity values. Red dots denote the shifted hypocenters and the resulting hypocenters are indicated with blue dots. (a) Latitude shift (km) (b) Longitude shift (km) (c) Depth shift (km).

Figure 4.7 indicates that the event mislocation in latitude and longitude is lower than 1 km with an average of 0.332 km in latitude and 0.326 km in longitude. These values state that majority of the shifted hypocenters closely recovered to their original locations after the simultaneous inversion. On the other hand, event mislocation in depth is between 0 and 5 km for most of the shifted hypocenters with an average of 2.56 km. Higher mislocation values might be caused by the uncertainties in the depth calculation of initial hypocenters. Figure 4.8 indicates the event mislocation in three coordinates for a fixed (highly overdamped) velocity model.

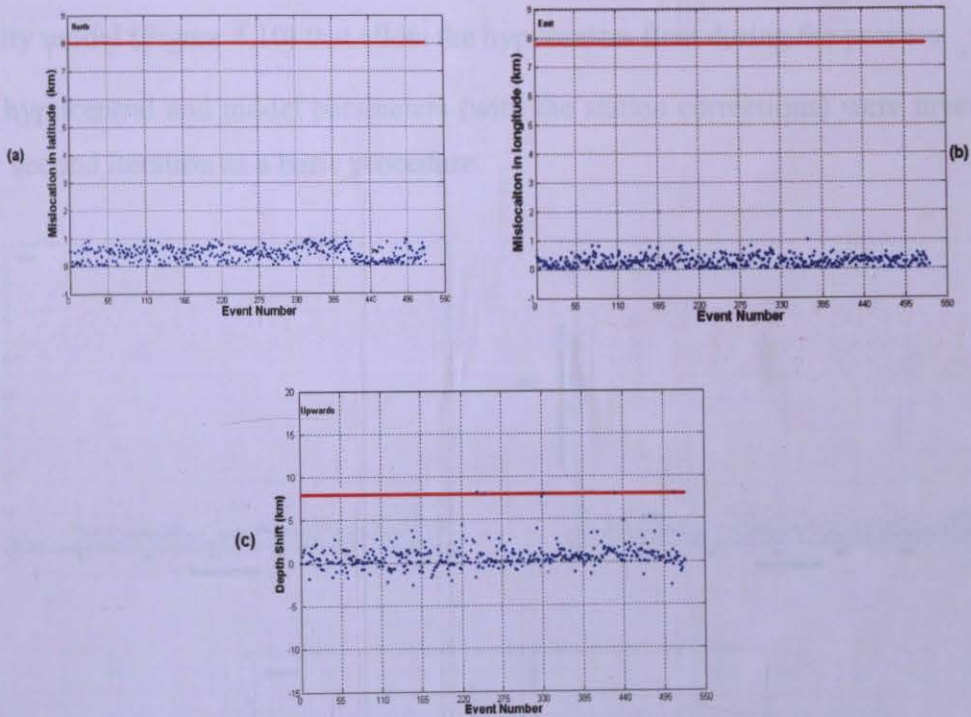


Figure 4.8. Inversion results after applying the constant shifting values for the fixed velocity values. Red dots denote the shifted hypocenters and the resulting hypocenters are indicated with blue dots. **(a)** Latitude shift (km) **(b)** Longitude shift (km) **(c)** Depth shift (km).

The event mislocation was also calculated lower than 1 km in general with an average of 0.342 km in latitude and 0.315 km in longitude, respectively. Mislocation in depth with an average of 2.39 km indicated an improvement compared to the previously mentioned damped velocity model. Despite the slight differences, these values state that the minimum velocity model is consistent within itself and majority of the shifted

hypocenters closely recovered to their original locations after the simultaneous inversion.

4.5.2 Random Shifting Test

Following the systematic shifting test, another stability test was performed by randomly perturbing the initial hypocenters 5-7 km in each direction. Latitude and longitude values are shifted to a certain positive value mentioned above, but the depth values are shifted both to positive and negative values. The simultaneous inversion with 15 iterations was performed both for a damped velocity model (Figure 4.9) and a fixed velocity model (Figure 4.10) that allow the hypocenters float during the process.

Both hypocentral and model parameters (with the station corrections) were inverted in every second iteration as a basic procedure.

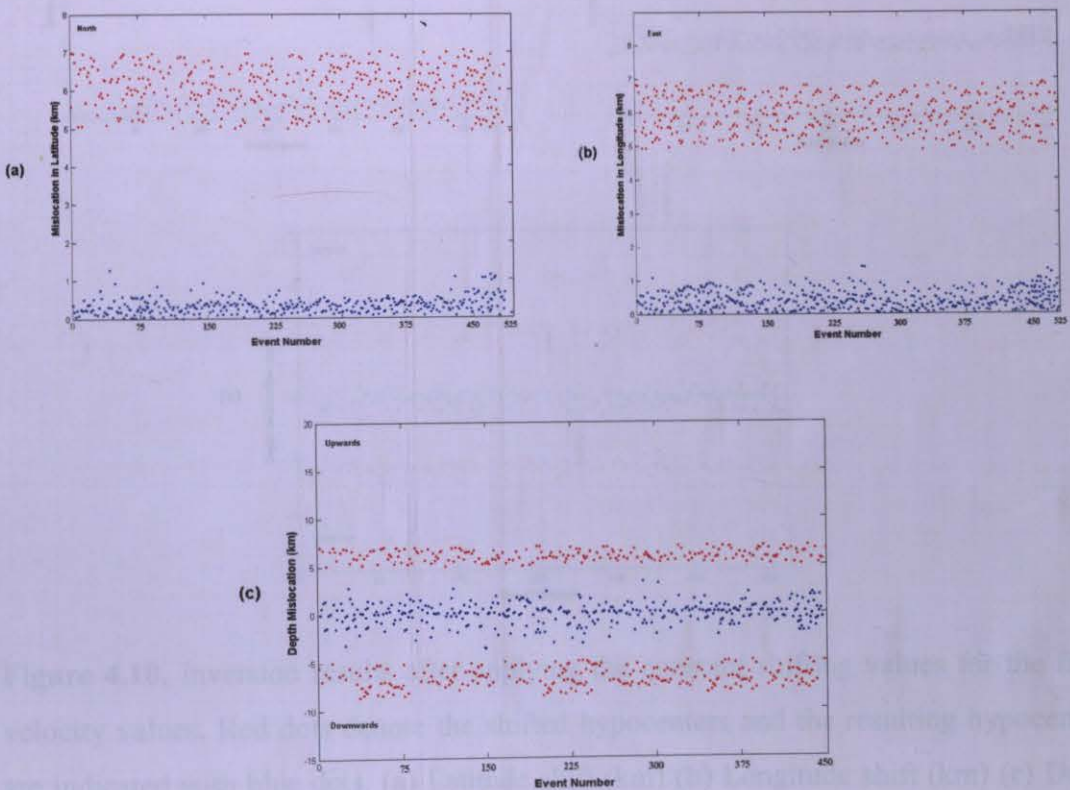


Figure 4.9. Inversion results after applying random shifting values for the underdamped velocity values. Red dots denote the shifted hypocenters and the resulting hypocenters are indicated with blue dots. (a) Latitude shift (km) (b) Longitude shift (km) (c) Depth shift (km).

Figure 4.9 suggests that, with a few exceptions, the majority of event mislocations in latitude and longitude is lower than 1 km with an average of 0.321 km in latitude and 0.336 km in longitude. We have observed a slight increase in longitude mislocation and a decrease in latitude mislocation compared to the systematic shift. On the other hand, event mislocation in depth is between 0 and 5 km for most of the shifted hypocenters with an average of 2.6 km.

Figure 4.10 indicates the event mislocation in three coordinates for a fixed (highly overdamped) velocity model with random shifting.

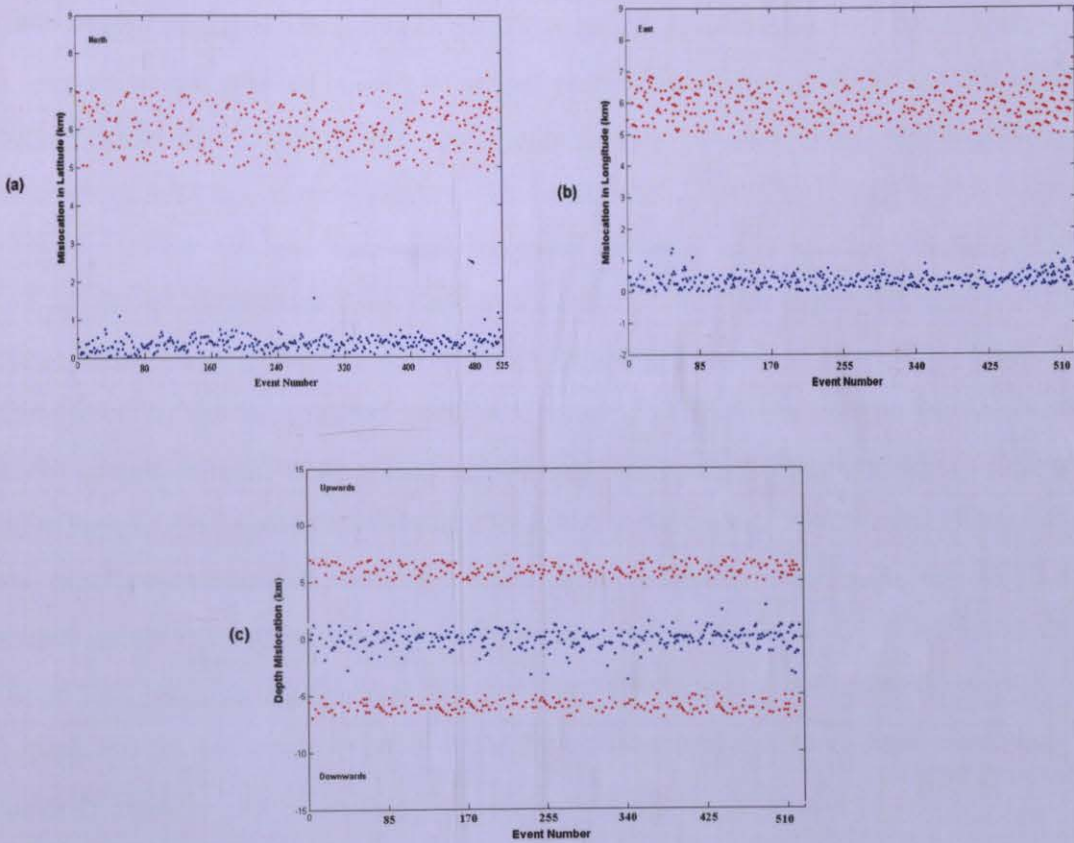


Figure 4.10. Inversion results after applying the constant shifting values for the fixed velocity values. Red dots denote the shifted hypocenters and the resulting hypocenters are indicated with blue dots. **(a)** Latitude shift (km) **(b)** Longitude shift (km) **(c)** Depth shift (km).

Using the fixed velocity model for the random event shifting, we observed a latitude mislocation of 0.304 km and a longitude mislocation of 0.315 km. The depth mislocation had the lowest value of 2.1 km. As seen in Figure 4.10, shifted hypocenters tend to return to their original positions as we also observed in the previous examples.

Consequently, after the random and the systematic event shifting tests overall mislocation results looked to be consistent within each other suggesting that “1-D minimum P-wave velocity model” has the sufficient resolving power in terms of model stability.

5. THREE DIMENSIONAL (3-D) VELOCITY TOMOGRAPHY

Local Earthquake Tomography (LET), or in general seismic velocity tomography, is a powerful technique to determine the 2-D/3-D velocity structure of the target volume using the travel times from accurately located local or teleseismic events. This method represents a linearized approximation to an originally non-linear problem.

Seismic velocity tomography is more difficult than medical tomography since seismic waves strongly interact with the structure being imaged and raypaths become one of the crucial parts of the problem. Main goal of LET is to improve the estimates of the model parameters (structure and hypocenters). The major advantages of LET over teleseismic tomography are; the potential for higher resolution imaging of the structure due to higher frequency content of local earthquakes, closer station spacing and the presence of sources within the model volume that generally allows for finer spatial sampling (Thurber 1993). On the other hand, the depth extent of LET models will be limited by the maximum earthquake focal depths in the area, while the depth extent of teleseismic tomography models can be of the order of the dimension of the array (Aki, 1982). Compared to the controlled-source tomography, LET offers substantial excitation of both compressional and shear waves and their three-dimensional (3-D) spatial distribution. An important drawback, however, is the lack of independent knowledge of the exact event locations and origin times. Another disadvantage is the variability of the model sampling caused by non-uniform earthquake source distribution. It should be noted that, both the resolution of the tomographic image and the solution quality heavily depend on the source-receiver distribution and the appropriate parameterization of the velocity field.

By using LET applications it is also possible to determine both the 3-D vertical and horizontal variations in a layered model, which will lead us to more accurate geologic and tectonic interpretations regarding the region under study. As mentioned in Chapter 1 several researchers around the world have examined the various aspects of the LET methodology in different regions (i.e., volcanoes and subduction zones etc.) with different types of treatments to the problem thanks to the simplicity and the uniformness of the theory. In this section, the basic theory of LET including the major aspects of the

problem and the tomographic application for ETSE network will be given in some detail.

5.1 Basic Let Theory

Following Thurber (1993), basic LET theory starts with the body wave travel time T from an earthquake i to a seismic station j that is expressed below using ray theory as a path integral,

$$T_{ij} = \int_{\text{source}}^{\text{receiver}} u ds \quad (5.1),$$

where u is the slowness field (reciprocal of velocity) and ds is an element of path length. The actual observations are the arrival times t_{ij} , where

$$t_{ij} = \tau_i + T_{ij}, \quad (5.2)$$

and τ_i is the earthquake origin time. The only known parameters in the LET problem are the receiver locations and the observed travel times (still including some uncertainty). The hypocentral parameters (x, y, z), origin times, ray-paths, and slowness field are known (the model parameters). The geometry of the problem is shown in Figure (5.1).

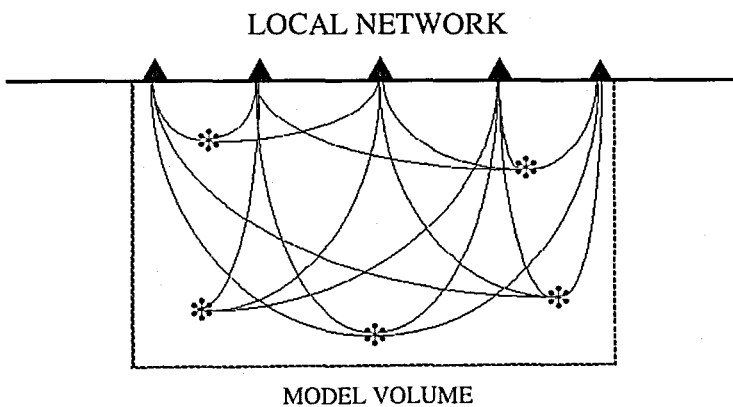


Figure 5.1. Schematic representation of the LET problem. Sources are distributed within the model volume (Thurber, 1993).

The calculated arrival times t_{ij}^{obs} are determined from equations (5.1) and (5.2) are the residuals r_{ij} ,

$$r_{ij} = t_{ij}^{\text{obs}} - t_{ij}^{\text{cal}} \quad (5.3)$$

The residuals can be related to the perturbations to the hypocenter and velocity structure parameters by a linear approximation,

$$r_{ij} = \sum_{k=1}^3 \frac{\partial T_{ij}}{\partial x_k} \Delta x_k + \Delta \tau_i + \int_{\text{source}}^{\text{receiver}} \delta u \, ds. \quad (5.4)$$

Equation (5.4) is valid for both P and S arrival time data. The hypocenter partial derivatives are proportional to the components of the ray vector times the slowness at the source point (Thurber, 1986):

$$\frac{\partial T_{ij}}{\partial x_k} = - \left[u \frac{dx_k}{ds} \right]_{\text{source}} \quad (5.5)$$

If a finite parameterization of the velocity structure is adopted, Equation (5.4) can be rewritten as,

$$r_{ij} = \sum_{k=1}^3 \frac{\partial T_{ij}}{\partial x_k} \Delta x_k + \Delta \tau_i + \sum_{l=1}^L \frac{\partial T_{ij}}{\partial m_l} \Delta m_l \quad (5.6)$$

where m_l represents the L parameters of the velocity model. The velocity model partial derivatives are the line integrals along the raypath.

All LET applications begin with equation (5.4) or (5.6) and these methods are based on the following aspects and different treatments of the problem:

- (a) the scheme for the representation of the velocity structure;
- (b) the technique for travel time and ray-path calculations;
- (c) the treatment of the hypocenter-velocity structure coupling;
- (d) the method of inversion (SIMULPS14-Damped Least Squares);
- (e) the assessment of solution quality;
- (f) the use of S waves.

The ray theory used in LET studies has its limitation regarding the ray theory, which assumes that these observed arrivals are the 'direct' ray theoretical arrivals. Seismic energy propagates through some finite volume surrounding a 'ray', not along an infinitesimal line. Diffracted arrivals with finite frequency may exist in reality that is not modeled by the ray theory (Wielandt, 1987).

5.1.1 Representation of the Velocity Structure

The Earth's crust and upper mantle displays a heterogeneous structure on a wide range of spatial scales, including discontinuities, faults, layering, intrusions and partial melt. Imaging this complex structure mainly depends on the density of ray sampling, proportional to the minimum wavelength of the recorded seismic wave energy (Thurber, 1993).

Different approaches can be mentioned to represent this heterogeneity. One of them is the constant velocity block approach of Aki and Lee (1976) that represents the earth as a set of boxes within each of which the velocity is constant (Figure 5.2(a)). This approach is simple but lacks in representing the complexity adequately. In terms of the inverse theory, block and layer methods are over-determined (more independent data than unknowns) and under-parameterized (insufficient parameters to present the real Earth). In addition, vast number of blocks usually leads to the problem being underdetermined (more unknowns than independent data) and increases the computational burden.

Discrete block parameterization also includes laterally varying layers (Hawley et al., 1981) and a 3-D grid of nodes (Thurber, 1983), as shown in figures (no: b, c). In the approach of Hawley *et al.* (1981), the model is divided into layers in which the velocity is constant in the vertical direction, but interpolated among vertical nodal lines in the horizontal directions. The block spacing may differ from layer to layer. Thurber (1983) used a 3-D grid approach, where the velocity changes continuously in all directions and linearly interpolated among the nodes.

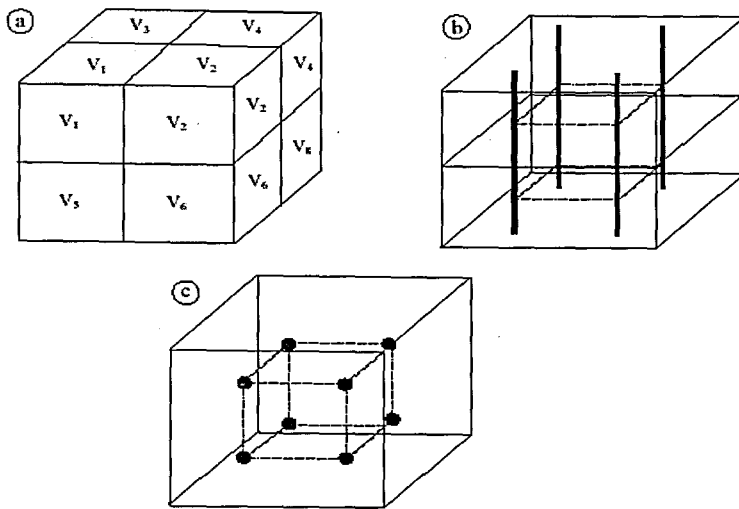


Figure 5.2. Geometry of three different approaches to velocity model representation: (a) constant velocity blocks, (b) laterally varying layers, (c) grid of nodes. Dashed lines indicate the spatial form of interpolation (Thurber, 1993).

There are also several different treatments relevant to this aspect of the LET problem. The advantage of the use of either the grid or ‘many block’ approach is their proven success. Being the ‘local solutions’, the perturbations in both of these approaches affect the velocity structure only in the vicinity (neighborhood) of the grid point or the block. All things considered, the appropriate approach should be selected taking into account the particular LET data set.

5.1.2 Ray-Path and Travel Time Calculation

One of the crucial aspects of LET is the determination of the propagation path between the each source-receiver pair and the travel time of the seismic wave along that path. Travel time is required to calculate the arrival time residual; the path is needed to compute the hypocenter and velocity model partial derivatives (Thurber, 1986). Ray tracing methods can be classified as ‘approximate’ and ‘exact’ methods. Shooting, Bending, approximate, finite difference methods can be classified as the ray tracing methods depending on being exact or approximate and the computational approaches to the problem.

Ray tracing is a two-point boundary value problem (BVP); the source and the receiver positions are specified and the propagation path must be determined. Shooting methods solve the two-point BVP by iteratively solving an initial value problem (IVP) with one fixed end point and the initial ray trajectory varied, while bending methods solve the BVP directly by keeping the end points fixed and perturbing the path connecting them. (Figure 5.3). Approximate ray tracing methods can introduce errors in the calculation of partial derivatives, residuals, but has the advantage in terms of computational speed.

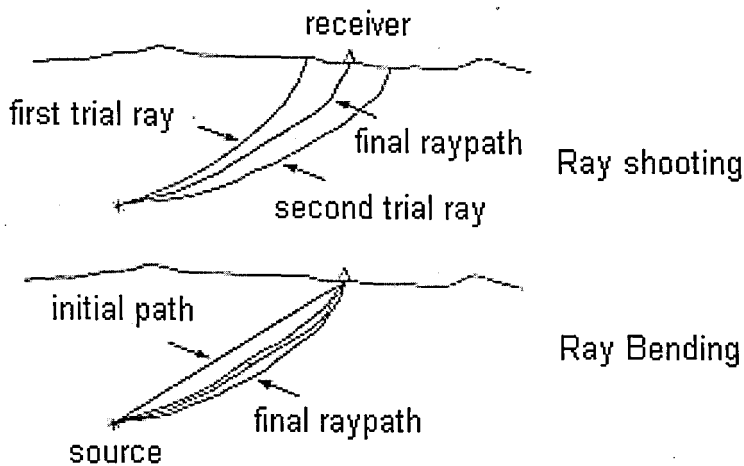


Figure 5.3. Schematic representation of the two ray tracing techniques: of ray shooting (top) and ray bending (bottom).

Both of these methods suffer from converging to a local travel time minima. Some of the shooting algorithms developed for LET are described by Koch (1985), Lin and Roecker (1990). Bending methods have been developed by Wesson (1971), Pereyra *et al.* (1980), among others. In this study, the pseudo-bending method of Um and Thurber (1987) and the shooting method of Virieux (1991) and Virieux and Farra (1991) are used as a part of the LET algorithm.

The original ray-tracing algorithm in SIMULPS14 is pseudo bending, where initial travel times are computed for a set of arcs connecting the source and the receiver. These arcs are of different radii and lay in planes dipping at different angles. The arc that yields the smallest travel time is chosen as an initial ray path (approximate ray tracing (ART), Thurber, 1983). Then, this path is perturbed by pseudo bending (Um and Thurber, 1987) by moving the ray segment endpoints in -the direction of the largest

velocity gradient. This method has been proven to work efficiently in most LET studies. However, significant inaccuracies may occur for ray paths exceeding 60 km length (Prothero et al., 1988).

The second ray-tracing scheme is a shooting and perturbation method, where the ray, which connects station and receiver, is found by varying initial azimuth and take-off angle at the source. The general theory is explained in Virieux (1991) and Virieux and Farra (1991). Introducing the slowness vector, shooting normally implies that the initial angles have to be adjusted so that so that the ray surfacing point reaches the station with a required accuracy using the paraxial rays (defined by the user). In the following this ray-tracing scheme will be abbreviated RKP-ray tracing (Runge-Kutta Perturbations). RKP method has given more accurate results for raypaths exceeding 60km (Hasslinger and Kissling, 2001).

5.1.3 Hypocenter –Velocity Structure Coupling

The mathematical coupling between hypocenter parameters and the velocity structure model is apparent in equation (6). The term local earthquake ‘tomography’ has usually implied the determination of 3-D velocity structure keeping hypocenter parameters fixed at their initial values, while ‘simultaneous’ inversion is usually construed to mean an explicit treatment of the hypocenter-velocity structure coupling (Thurber, 1993). The issue is whether to ignore this coupling or not. The complete system of inversion equations can be written as:

$$\mathbf{r} = \mathbf{H}\Delta\mathbf{h} + \mathbf{M}\Delta\mathbf{m}, \quad (5.7)$$

where \mathbf{r} is the residual vector, \mathbf{H} and $\Delta\mathbf{h}$ are the matrix and vector of hypocenter parameter partial derivatives and perturbations, respectively, and \mathbf{M} and $\Delta\mathbf{m}$ are the matrix and vector of velocity parameter partial derivatives and perturbations, respectively. In geologically complex regions, ignoring the hypocenter-velocity structure coupling; that is, the term $\mathbf{H}\Delta\mathbf{h}$ in equation (5.7) will inevitably result in systematic bias in the velocity model that will lead to hypocenter mislocation.

Furthermore, parameter separation was used by Pavlis and Booker (1980) as the practical technique to treat this coupling implicitly. This method is effective when the estimated hypocenters are linearly close to their true locations.

In other studies, Kissling (1988) has tested the need for the parameter separation step and he found that ignoring the hypocenter-velocity structure coupling ends up with a severely biased model. In a similar analysis, Thurber (1981 and 1992) indicated a significant improvement in the model fidelity when the hypocenter-velocity structure coupling was included in the inversion equations.

5.1.4 The Method of Inversion and Simulps14 Algorithm

One of the major difficulties in LET is to handle the non-linearity of the problem. LET inversion can be intractable due to the high level of heterogeneity in the structure and the large size of the matrix involved. In this case, it is essential to adopt an iterative approach to finding a solution. With the increasing power of computers, these equations could be solved via Singular Value Decomposition (SVD) (Lawson and Hanson, 1974) which breaks down the matrix in equation (5.6) into a product of three orthogonal matrices containing the singular vectors of the data and model spaces and the corresponding singular values.

A common alternative to SVD is the Damped-Least Squares approach with the combination of parameter separation (Pavlis and Booker, 1980). “Damped-least Squares” means that the norm of the model perturbations is weighted and combined with the squared data misfit. The combination is minimized at each iteration (SimulPS14 Manual). Equation (5.6) can be rewritten in matrix notation as:

$$\mathbf{G}\Delta\mathbf{m} \cong \Delta\mathbf{d}. \tag{5.7}$$

The vector $\Delta\mathbf{d}$ contains the residuals for the observations, the matrix \mathbf{G} contains the partial derivatives hypocentral and velocity parameters, and the vector $\Delta\mathbf{m}$ contains the model adjustments. Thus, a perfect fit of the data will be never reached even with the perfect data. Because of the non-uniform ray sampling and distribution, equation (5.7) is a mixed determined problem. To avoid very small or zero eigenvalues for the underdetermined model parameters, damping is introduced to stabilize the numerical solution (Menke, 1989).

The solution to this inverse problem is obtained with the construction of the normal equations and the addition of the damping factor using the equation,

$$\Delta\mathbf{m} \approx [\mathbf{G}^T\mathbf{G} + \lambda^2\mathbf{I}]^{-1}\mathbf{G}^T\Delta\mathbf{d}, \tag{5.8}$$

resulting in a matrix size fixed by the number of velocity model parameters. “**T**” is the unity matrix and λ is called the damping factor.

In this study, we used the SIMULPS14 version of the LET algorithm originally written by Thurber (1983, 1993) and updated by Eberhart-Philips (1986, 1990). SIMULSPS14 algorithm uses the damped-least-squares approach and the parameter separation technique (Pavlis and Booker, 1980) in order to solve the nonlinear LET problem. Parameter separation splits **G** into two matrices **H** and **V**, one containing the hypocentral partial derivatives (**H**) and the other containing the model partial derivatives (**V**). After parameter separation, equation (5.8) becomes for the model parameter part:

$$\Delta V \approx (V^T V + \lambda^2 I)^{-1} V^T \Delta d'. \quad (5.9)$$

Using parameter separation, earthquakes are currently relocated separately with the updated velocity model after the inversion of the model parameters. The solution of the equation (5.7) heavily depends on the choice of the initial model parameters and hypocenters.

The damping factor (λ) strongly affects the solution and depends on source-receiver distribution and grid spacing. Low damping values will lead to a high model variance, whereas high damping values will lead to a smooth solution without a significant decrease in data variance. Appropriate damping value can be selected by evaluating trade-off curves based on single-iterations between the data and the model (solution) variance (Eberhart and Philips, 1986).

5.1.4.1 Model Parameterization in SIMULPS14

The correct assessment of model parameterization in seismic tomography is a difficult task since solution and solution quality (resolution estimates) are highly affected by the chosen model parameterization. Model parameterization must account for *a priori* knowledge of Earth’s structure and the resolution capability of the available data set (Kissling et al., 2001). Dense grid spacing is required to represent structures such as sedimentary basins or Moho topography, but on the other hand coarse-grid spacing is needed by nonuniform ray coverage. Unevenly spaced models make the interpretation of the tomographic results and solution quality more complicated due to velocity

smearing between the grid nodes. In terms of solution quality, coarse grid spacing yields large-resolution estimates, whereas fine grid spacing yields low-resolution estimates. Station and earthquake distribution plays an important role in determining the type of node-grid geometry.

The velocity model in SIMULPS14 is parameterized by grid nodes defined at intersecting lines with variable spacing (Figure 5.4). V_p and V_p/V_s values are defined at each grid node in x-, y-, z- directions and values in between are linearly interpolated.

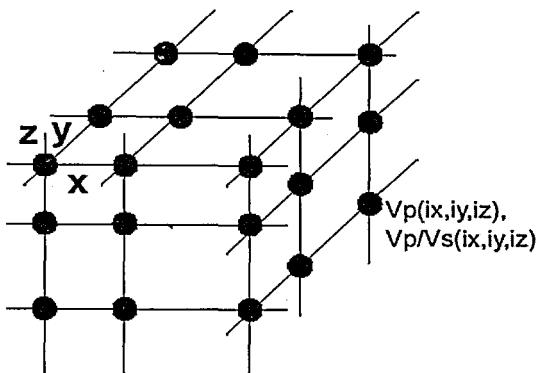


Figure 5.4. Node-grid geometry in SIMULPS14. Grid spacing may not be equal to account for the heterogeneities in the structure (Thurber, 1993).

Depending on the ray geometry, grid nodes can be either fixed by a threshold value for the minimum number of rays passing through a grid node. There also must be planes of nodes around all sides of the model, including top, bottom, any four sides placed effectively at infinity (i.e., several hundred km away). However this requirement may lead to long columnar velocity anomalies around the periphery of the array. For the RKP ray tracing the model has to be parametrized as squared slowness, and cubic B-spline interpolation is used to obtain these values. The grid representing for the squared slowness has to be equidistantly spaced in each direction. Cubic B-spline interpolation uses the four next neighbors in each direction (Figure 5.5).

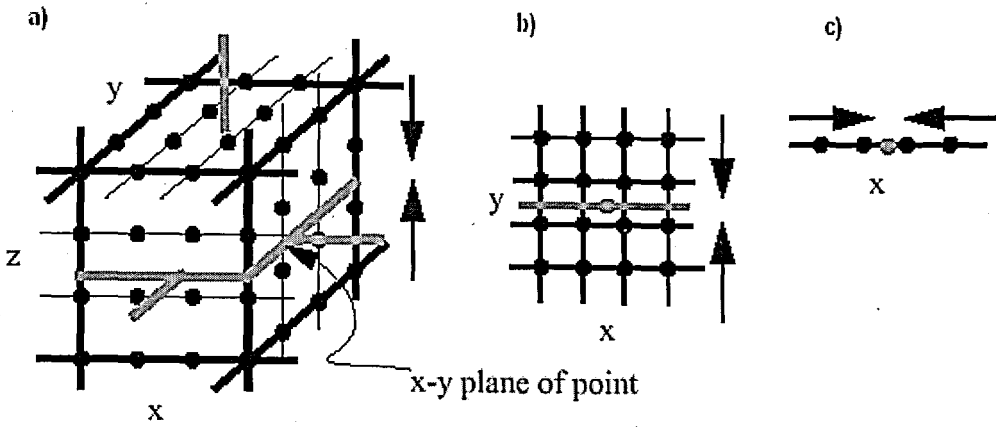


Figure 5.5. Scheme for 3D cubic B-spline interpolation. The solid black circles are the control values (grid nodes) and the grey circle is the target point. **a)** Interpolation along z onto x - y plane of point. **b)** interpolation along y onto x -coordinate of point. **c)** Interpolation along x onto point (Kissling et al., 2000).

5.1.5 Solution Quality

Interpretation of the tomographic results primarily depends on the solution quality in terms of several measures such as data variance (misfit), resolution estimates and model covariance. Misfit is a measure of disagreement between the observed and predicted data; resolution indicates the interdependence of the predicted model parameters and covariance measures the mapping of data errors on to model parameter errors.

In the discrete inverse theory approach, in case of obtaining the solution to the problem $\mathbf{G}\Delta\mathbf{m} \cong \Delta\mathbf{d}$, an inverse \mathbf{G}^{-1} is computed. The matrices of model resolution \mathbf{R} and model covariance \mathbf{C}_m can be calculated by the following equations:

$$\mathbf{R} = \mathbf{G}^{-1}\mathbf{G} \quad (5.10)$$

$$\mathbf{C}_m = (\mathbf{G}^{-1})^T \mathbf{C}_d \mathbf{G}^{-1} \quad (5.11)$$

where \mathbf{C}_d is the data covariance matrix (Menke, 1989). \mathbf{C} contains the estimated variance of individual parameters (diagonal elements) and the covariation between pairs of parameters (off-diagonal elements). Resolution and covariance matrices provide mathematical resolution estimates, where as weighted ray lengths (Thurber, 1983; Eberhart-Philips, 1986) or ray density tensors (Kissling, 1988) illustrate the illumination properties of the data set. However, these resolution estimates are related to the assumed model parameterization and do not assess the validity of this parameterization. The best

ways to study the effects of a particular model parameterization, forward or inverse solution are the synthetic data tests using a synthetic 3-D velocity model (Husen and Kissling, 2000; Hasslinger and Kissling, 2000). The tests with the synthetic data and the characteristic resolution parameters in SIMULPS14 algorithm with the actual data will be described in section 5.3.

5.1.6 Use of Shear (S) Waves

We can make a more complete characterization of the crust and upper mantle regarding their geologic and geophysical features, if P and S velocity structures are combined efficiently (Eberhart-Philips, 1989,1990). S waves also provide useful information and increases constraints on the earthquake source depths.

However, in practice, the use of S waves in LET applications is rather limited due to a lack of three-component data. In addition; S phase arrives within the P phase coda, is more attenuated than P, has S-P converted phases, and exhibits polarization and splitting due to anisotropy.

In SIMULPS14 algorithm, S phases along with the P phases are used to derive V_p/V_s velocity structure instead of a separate V_s velocity model. Inverting for V_p/V_s instead of V_s is based on the assumption that in areas of lower V_s resolution and high V_p resolution, V_p/V_s is better estimated from an initial average V_p/V_s value than from a homogeneous V_s model (Eberhart-Philips and Reyners, 1997). This is of great importance for data sets with significantly fewer S than P phases, which is often the case in most LET applications. V_p/V_s ratio is directly related to the Poisson's ratio. The treatment of S waves is no different than P waves. If V_p/V_s is treated as a constant initially, the observed S-P time difference dt_{ij} can be expressed as,

$$dt_{ij} = \int_{\text{path}} [(V_p/V_s) - 1] / V_p ds, \quad (5.12)$$

Expected S-P times are calculated using the 3-D P wave velocity model and constant V_p/V_s value. Then the S-P time residuals $\Delta t_{ij} = dt_{ij} - dt_{ij}^*$ are related to perturbations to V_p/V_s at the nodes of the 3-D grid, and are inverted for V_p/V_s in a single step, keeping the V_p values and hypocenters fixed (Thurber, 1993). S waves are not included in this study due to insufficient number of clear phase readings on the waveforms due to high attenuation (Gök, 2003).

5.2 3-D Tomographic Applications for Eastern Turkey

5.2.1 Data Selection

A total number of 504 events and the corresponding station corrections from VELEST algorithm were used as initial earthquake locations for the three-dimensional (3-D) tomographic inversion (Figure 5.6). Data selection criteria were identical with the previously performed one-dimensional (1-D) velocity inversion except the azimuthal gap. Azimuthal gap value of the LET data set is $< 180^\circ$. This additional criterion reduced the number of events from 523 to 504 (6742 P-phase readings).

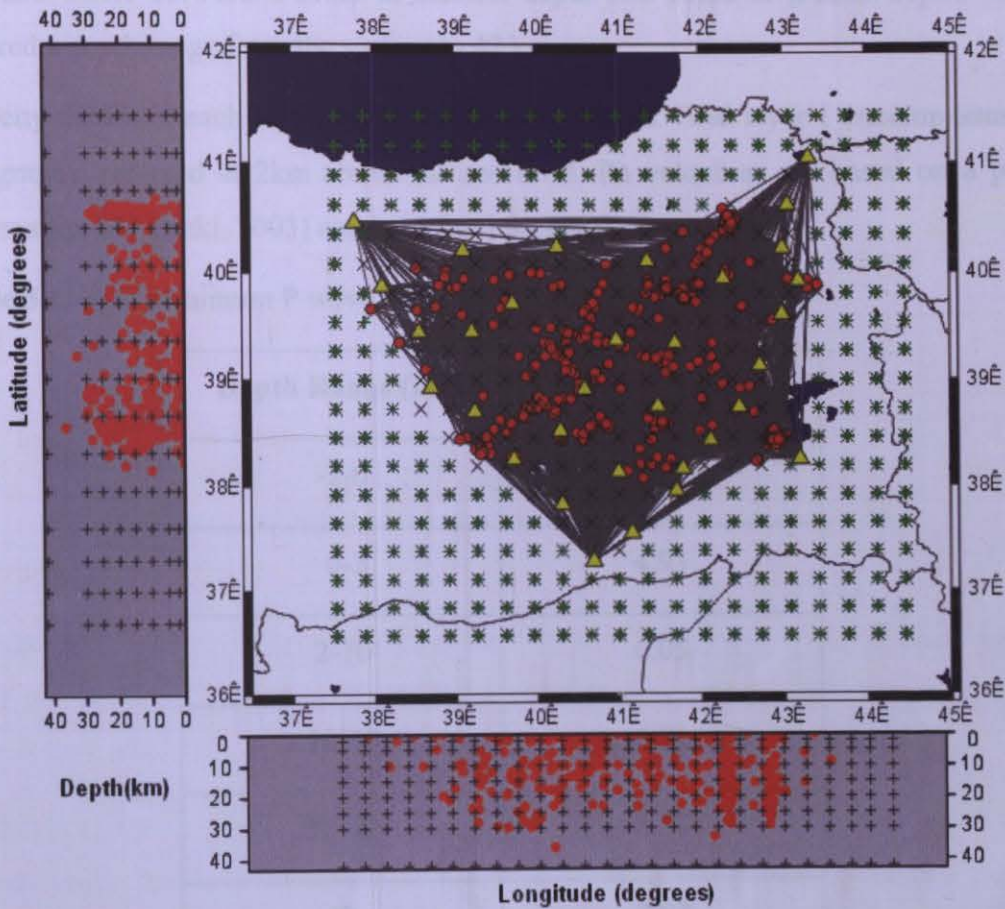


Figure 5.6. Selected event locations for the tomographic inversion along with the depth distribution in latitude and longitude cross-sections. Yellow triangles represent the stations, red circles represent the events, green signs represent the nodes that were held fixed in the inversion, black crosses indicate the nodes used in the inversion and the theoretical ray-paths are shown with gray lines.

5.2.2 Model Parametrization

Model Parameterization and resolution estimates in SIMULPS14 were explained in detail in section 5.1.4.1. The velocity model was parametrized by grid nodes with variable spacing. Grid node spacing should be chosen to adequately represent the expected structure and to allow uniform resolution throughout the model.

Considering the station spacing and the ray distribution of the selected data, a horizontal grid with 30x30 km node spacing was chosen for the 3-D inversion. Vertical grid spacing (grid spacing at depth) was taken from the 1-D minimum velocity model (Table 5.1) and varies between 2-5 km at shallow depth and 10km at greater depth, which covered a depth range from the surface to 42 km.

Velocity values at each layer are uniformly constructed. Grid layer 1 encompasses the topography centered at 2km above the sea level. Pn velocities are based on a priori information (Al Lazki, 2003) and held fixed during the inversion.

Table 5.1. 1-D Minimum P wave Velocity Model

Depth Range (km)	Velocity (km/sec)
-2-0	3.57
0-2	4.93
2-10	6.05
10-30	6.21
30-42	6.37
42-	7.83

Using this parameterization, we can derive a coarse but reliable image of the 3-D crustal structure. Velocity values were held fixed at grid nodes, which were not hit by any rays. In this study, we chose to define the solution as reliable if the model parameter belongs to an area that is well illuminated, as measured by the main resolution parameters such

as Derivative Weight Sum ($DWS > 1000$), and shows uniformly high resolution as measured by the Resolution Diagonal Elements ($RDEs > 0.2$).

5.2.3 Control Parameters

Damping factor (λ) is one of the most critical factors of the tomographic inversion. The choice of damping values for the 3-D inversion was based on a series of tests on the trade-off between the model variance, and data variance (Eberhart-Philips, 1986). For a large range of damping values, single iteration inversions were performed (Figure 5.7).

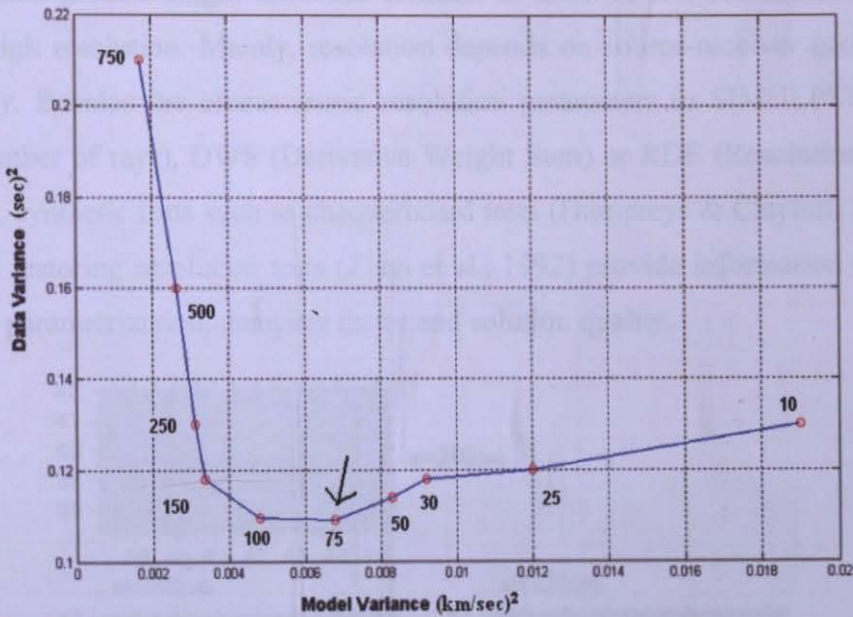


Figure 5.7. Trade-off curves indicating the model variance versus the data variance after one iteration. From this curve “75” was selected as the appropriate damping value shown with a black arrow.

A damping value of 75 was chosen from these tests, which led to a considerable reduction in the data variance with only a moderate increase in model variance (roughness). Depending strongly on source-receiver distribution and on grid spacing, damping affects not only the final solution but also the absolute values of the resolution matrix.

5.3 Solution Quality Assessment

The final data set of 504 events with 6742 P-phase arrival times were inverted to derive the 3-D P-wave velocity structure of Eastern Turkey using the appropriate model

parametrization, ray tracing technique, control parameters (damping and residual weighting parameters) and source-receiver distribution. It should be taken into account that tomographic results will be more reliable if resolution tests with the synthetic data are performed. In accordance to this procedure, the tomographic results for the actual data will be represented following the resolution tests with the synthetic data and the resolution parameters obtained by the real data.

5.3.1 Resolution Assessment with Synthetic Data

3-D inversion process might introduce artifacts in areas of low resolution or even in areas of high resolution. Mainly, resolution depends on source-receiver geometry and ray density. Besides the characteristic resolution parameters in SIMULPS14 such as KHIT (number of rays), DWS (Derivative Weight Sum) or RDE (Resolution Diagonal Elements), synthetic tests such as chequerboard tests (Humphreys & Clayton, 1988; Zelt, 1988) and restoring resolution tests (Zhao et al., 1992) provide information relevant to the model parametrization, damping factor and solution quality.

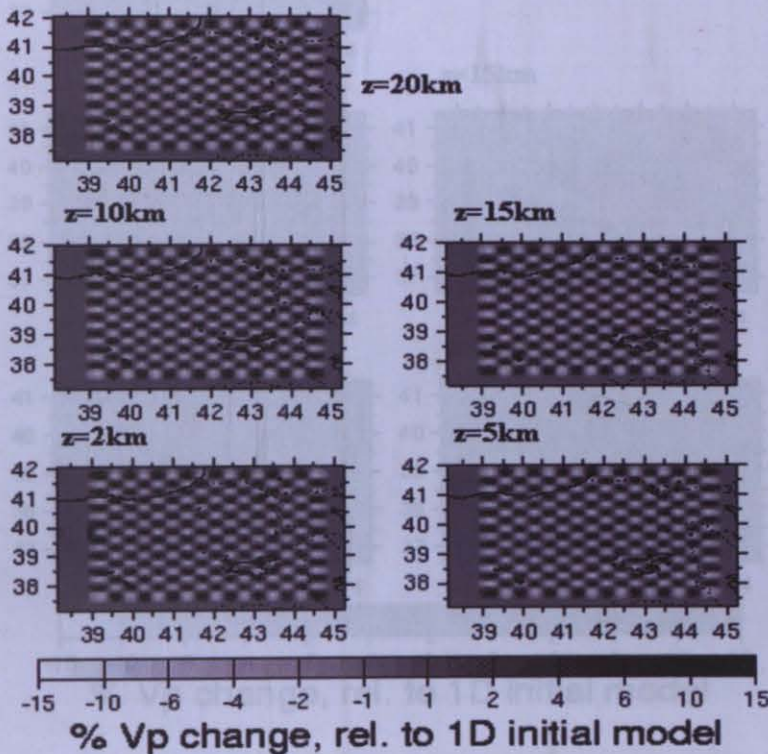


Figure 5.8. Horizontal depth sections of inversion results for the synthetic data set. P-wave velocity perturbations are shown relative to the 1-D minimum reference model. Black triangles represent the grid nodes used in the inversion.

Chequerboard tests are intuitive, however, they give only good estimates of the amount of velocity smearing. Chequerboard tests do not imply that large-scale structures are resolved as well as a fine-scale structure. In restoring resolution tests, inversion results are used as an input model during the calculation of synthetic travel times. This might also introduce the drawback that areas of low resolution might be identified as areas of high resolution due to fine recovery of the input model. To start with, we designed a synthetic chequerboard model with velocities %10 higher and lower than the minimum model (Figure 5.8).

Synthetic travel times were inverted using the identical model parametrization, control parameters and ray tracing technique as for the real data. Results for the 3-D inversion of the synthetic data are shown in Figure 5.9.

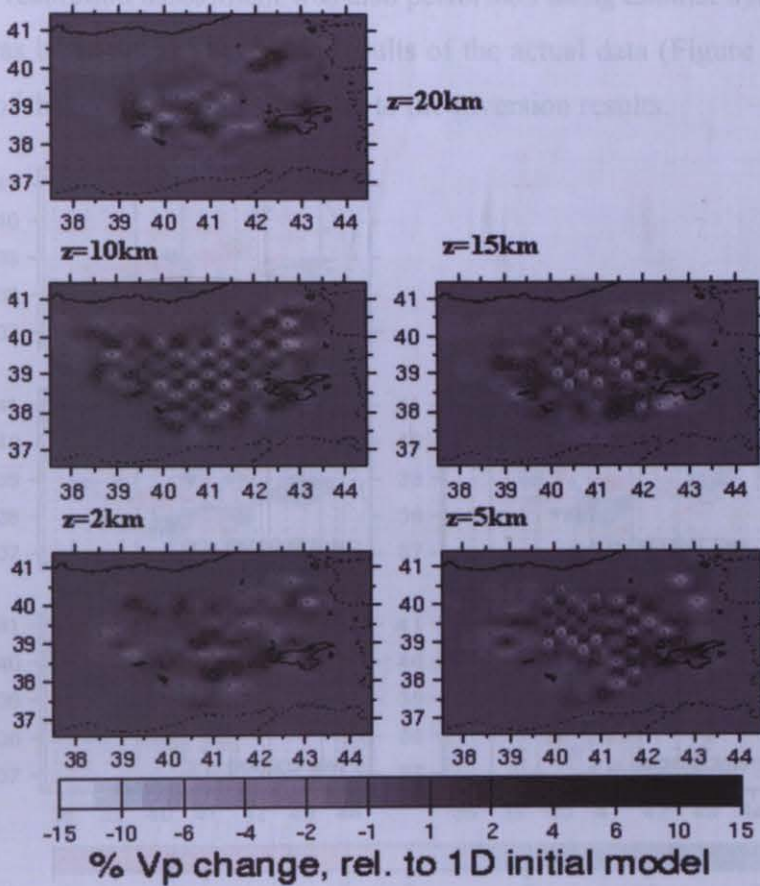


Figure 5.9. Horizontal depth sections of inversion results for the synthetic data set. P-wave velocity perturbations are shown relative to the 1-D minimum reference model. Red circles represent the events, yellow triangles represent the stations and black triangles indicate the grid nodes used in the inversion.

As mentioned in Figure 5.9 the damping effect is apparent in slightly reduced amplitudes of the recovered anomalies. We could suggest that initial anomalies are well recovered in grid layers down to 15km indicating a good resolution with a certain amount of velocity smearing. Resolution in grid layer of 20 km is much more affected by velocity smearing and relatively lower resolution is caused by insufficient number of earthquakes and sparse sampling in this depth range. In each layer, the central part of the network is well resolved compared to the outer parts. Resolving power for the outer parts of the network is lower as expected since the earthquake distribution is more heterogeneous in those areas. The effects of damping are generally reduced amplitudes of the recovered anomalies. Lower damping values would increase the amplitude recovery but stronger smearing effects would be more apparent.

Furthermore, resolution assessment was also performed using another synthetic velocity model that was based on the inversion results of the actual data (Figure 5.10). The size and the sign of the anomalies were similar to the inversion results.

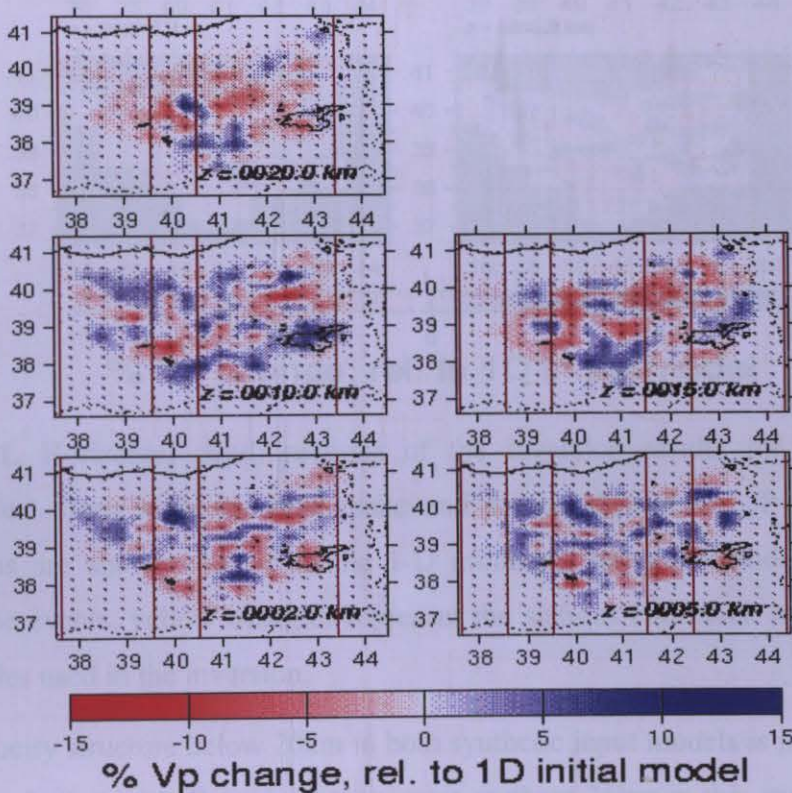


Figure 5.10. Horizontal depth sections of the synthetic velocity model based on the inversion results of the actual earthquake data. P-wave velocity perturbations are shown relative to the 1-D minimum reference model. Black triangles represent the grid nodes.

Inversion results of the synthetic resolution test were represented in Figure 5.11 with the earthquake and the station distribution. As seen in Figure 5.11, anomalies of the input synthetic model was again well retained with slightly reduced amplitudes suggesting that the resolving power is good inside the network and the amplitude recovery of initial velocity pattern decreases after 15 km depth range.

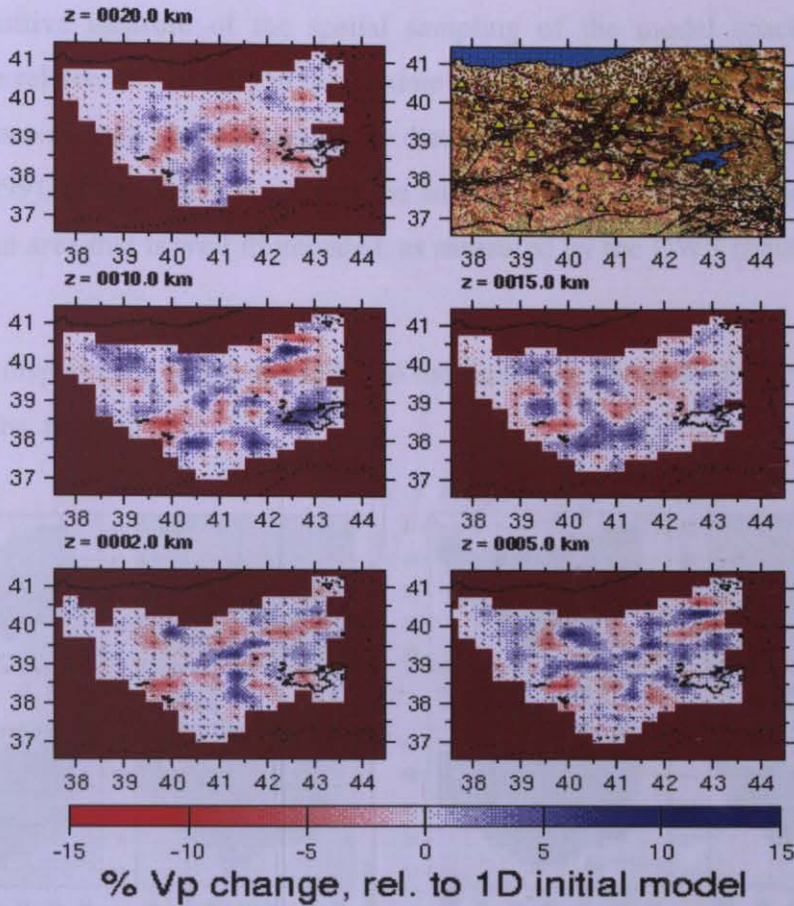


Figure 5.11. Horizontal depth sections of the inversion results for the synthetic resolution test along with the earthquake and station distribution. P-wave velocity perturbations are shown relative to the 1-D minimum reference model. Red circles represent the events, yellow triangles represent the stations and black triangles denote the grid nodes used in the inversion.

P-wave velocity structure below 20km in both synthetic input models is poorly resolved due to lack of seismicity. Seismicity terminates at about 25km in this study with a few exceptions.

5.3.2 Resolution Parameters of Real Data

In SIMULPS14 algorithm, the resolution estimates contain three important parameters, which are classified as the hitcount (KHIT), the derivative weight sum (DWS) and resolution diagonal elements of the resolution matrix (RDEs). KHIT denotes the number of rays that contribute to the solution at one node. The DWS is implemented as a more sensitive measure of the spatial sampling of the model space. The DWS indicates the relative ray density in the volume of influence of a model node, weighting the importance of each ray segment by its distance to the model node (Hasslinger and Kissling, 1999). In this study, we define the solution as reliable if the model parameter belongs to an area that is well illuminated, as measured by the DWS (>800), and RDEs (>0.2).

Figure 5.12 displays the KHIT and DWS of the final 3-D V_p model for several layers 2 -20 km depths, respectively.

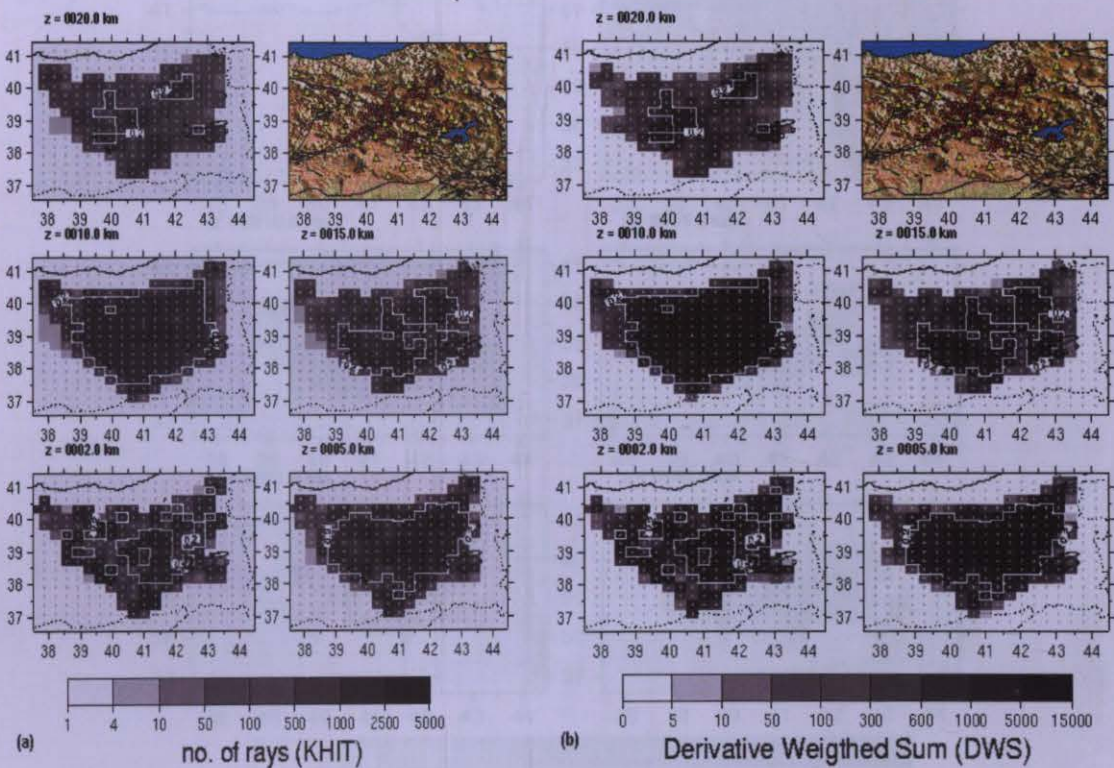


Figure 5.12. Horizontal depth sections of (a) KHIT and (b) DWS for the final V_p model. Events are shown by red circles, stations are shown by yellow triangles and small crosses denote grid nodes. White contour surrounds the area of reliable resolution (RDEs > 0.2).

We observed a more homogeneous distribution of high KHIT and DWS in the central parts of the model with increasing depth up to 20 km. This appears to be consistent with the resolution estimates for this region by the synthetic tests. Above 2 km depth range the resolution is relatively poor because of the sub-vertically traveling rays underneath the stations.

A more powerful measure regarding the assessment of the solution quality is the Resolution matrix (R). The rows of R describe the dependency of the solution for one model parameter on all the other model parameters. The RDEs also show the amount of independence in the solution for one model parameter. If the RDE is larger for one model parameter, the solution is more independent for this parameter. A more detailed discussion on resolution estimates is given in Toomey and Foulger (1989).

Figure 5.13 displays RDE distribution of the final 3-D Vp models in 2-20km ranges.

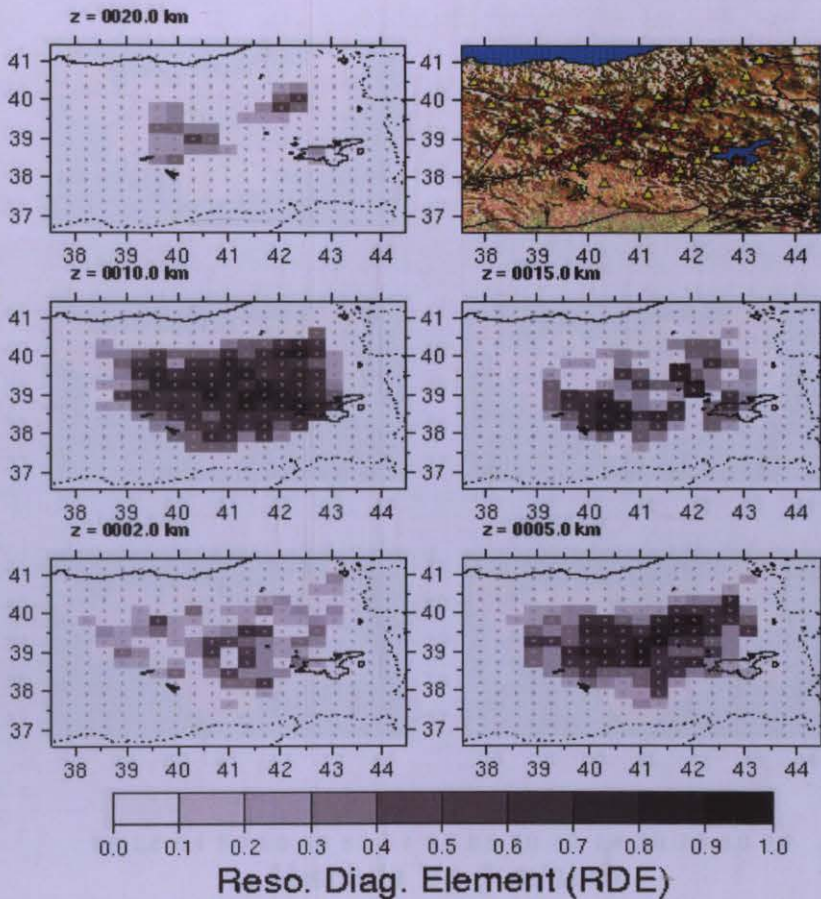


Figure 5.13. Horizontal depth sections of RDEs for the final Vp model. Red circles and yellow triangles represent the events and stations, respectively. Small crosses denote the grid nodes.

RDE distribution is also homogeneous except the grid layer at 20 km that indicates significantly lower resolution compared to other depth ranges. We calculated a highest value of 0.88 for RDEs in 5km and 10km depth ranges where the majority of seismicity is concentrated. RDE value is supposed to be “1” in ideal case indicating a perfect resolution. Below 20 km, resolution is poor due to sparse sampling, which is not presented in this study. It can be noticed that KHIT alone gives no information relevant to the reliability of the resolution assessment.

5.4 Results of 3-D Inversions

After five iterations and two processing steps, the final tomographic model for Eastern Turkey achieved a data variance reduction of $\sim 55\%$ (0.095 sec^2) and an average residual reduction of $\sim 50\%$ (0.18 seconds), respectively. Figures 5.14 and 5.15 display the absolute Vp distribution and velocity perturbations (%) relative to 1-D initial model for-

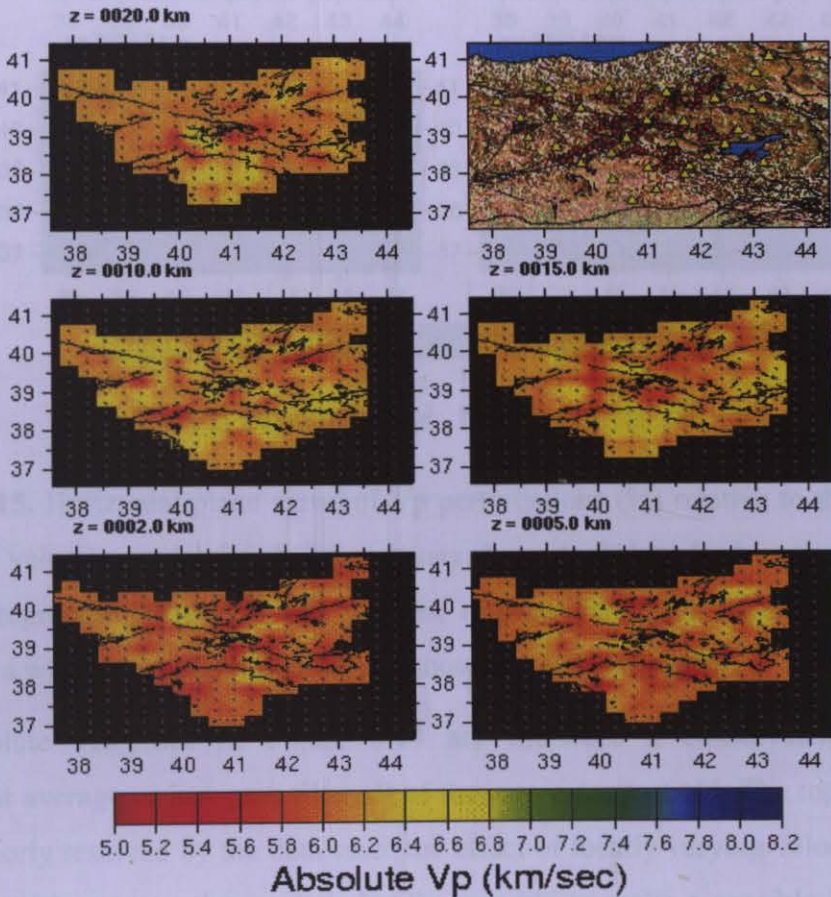


Figure 5.14. Horizontal plane views of absolute Vp distribution for different layers down to 20km. Major faults are shown by black lines. Red circles and yellow triangles represent the events and stations, respectively. Small crosses denote the grid nodes.

different layers centered up to 20km along with the station-event geometry. Areas of less reliable resolution ($DWS < 20$ and $KHIT < 10$) are shaded. Thick white contours denote the areas of more reliable resolution ($RDEs > 0.2$) in Figure 5.15.

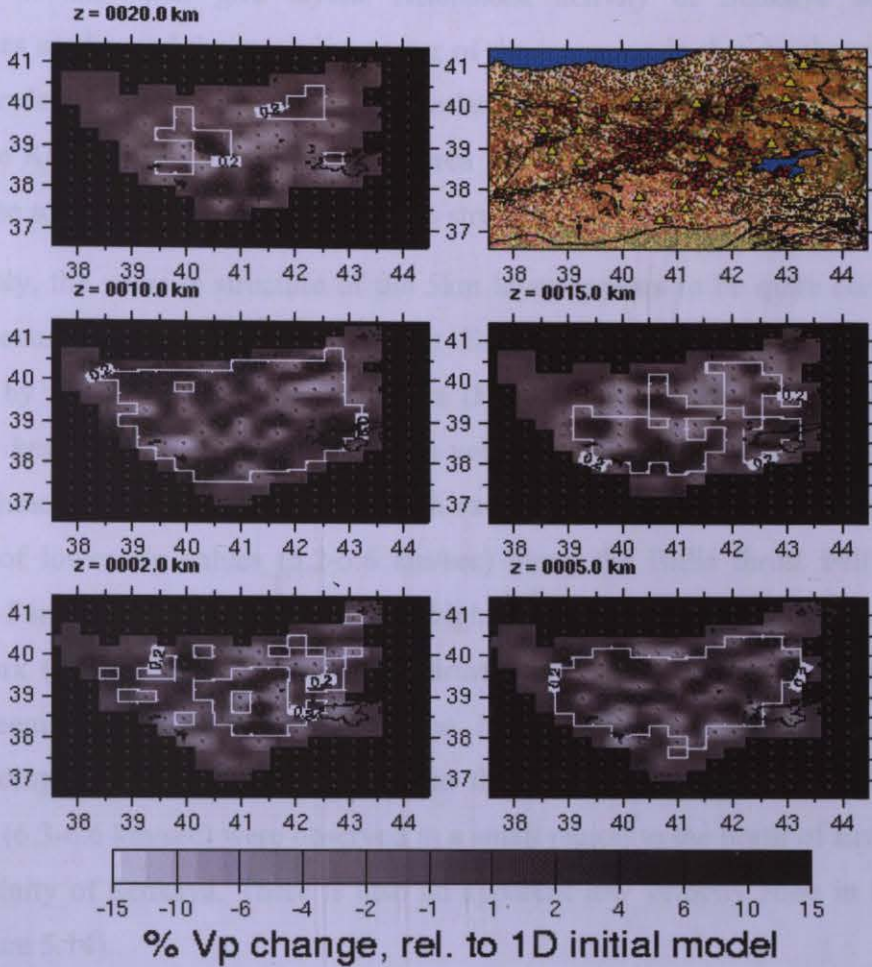


Figure 5.15. Horizontal plane views of V_p perturbations (%) relative to the initial 1-D minimum velocity model for different layers down to 20km. Red circles and yellow triangles represent the events and stations, respectively. Cells with $RDE > 0.2$ are shown by a white contour. Grid nodes are shown by white triangles.

The absolute velocities in Figure 5.14 are therefore a conservative estimation (somewhat average or low-pass filtered) of the true velocity field. The top layer above 2km is poorly resolved by the data since the effect of locally varying velocities may be compensated by station delays. It is hardly possible to make a sensible interpretation regarding this sedimentary layer and the surface geology due to sparse sampling and poor resolution.

Looking at Figure 5.14 and 5.15 together, V_p values vary from 5.48 km/sec to 7.07 km/sec corresponding to \sim -9.4 and %15 velocity change relative to the background velocity of 6.05 km/sec in grid layer at 2km where the resolution is relatively lower compared to the other grid layers. Aftershock activity of Senkaya and Gevas earthquakes are beyond the resolving power of the inversion in this depth range due to the deeper depth distribution. We observe relatively lower V_p values (5.2-5.6 km/sec) around the Karliova junction and a small area with higher V_p values (6.4-6.8 km/sec) towards the south reflecting a heterogeneous structure.

Comparably, the velocity structure of the 5km layer appears to be quite complex and heterogeneous similar to the grid layer at 2km with a more reliable resolution as indicated by figure 5.15 and synthetic tests (Figures 5.9 and 5.11). V_p values range from 5.41 km/sec to 6.63 km/sec. The high velocity anomaly towards the south of the Karliova junction disappeared in this depth range and displays a more homogeneous structure of lower V_p values (5.2-5.6 km/sec) along the Bitlis thrust belt and East Anatolian Fault Zone (EAFZ) with slightly higher values towards the southern border of the network (Figure 5.14). Towards the northern part of the network, lower velocity pattern seems to be dominant along the North Anatolian Fault Zone (NAFZ) corresponding to \sim -8% change relative to the initial model (Figure 5.15). Higher velocities (6.3-6.6 km/sec) were observed in a small region to the north of Erzincan and in the vicinity of Senkaya. There is also an apparent low velocity zone in Kağızman fault (Figure 5.14).

In the upper 10km range, combination of higher and lower velocity patterns were obtained from the inversion where the majority of the seismicity is concentrated throughout the well-resolved area (Figure 5.14 and 5.15). In this layer, V_p values vary between 5.40 km/sec to 7.0 km/sec. In this depth range, Bitlis Suture separates the lower velocity zone (5.5-5.9 km/sec) to the north including the Karliova junction and higher velocities (6.2-6.7 km/sec) to the south. Seismicity is also much more active to the north than to the south of the Bitlis thrust belt. Aftershock sequence of Gevas earthquake lies within the well-resolved area indicated by the white contour in Figure 5.15. We observed constant velocities of \sim 6.35 km/sec surrounding the Lake of Van corresponding to a \sim 7% velocity increase with respect to the initial velocity of 6.21 km/sec (Figures 5.14 and 5.15). Farther to the northeast, a lower velocity zone is located

excluding the aftershocks of Senkaya earthquakes that display a higher velocity anomaly (6.3-6.6 km/sec). Towards the southeast border of the network, a zone with slightly higher velocities was observed along the NAFZ.

In grid layer at 15 km, distinct higher and lower velocity patterns with a relatively lower amount of smearing were observed in both figures 5.14 and 5.15. V_p values change from 5.62 km/sec to 6.8 km/sec (Figure 5.14). Higher velocities similar to the grid layer of 10km are apparent to the south of Bitlis Suture, decreases towards the north including the Karliova junction. Lower velocities (5.6-6.0 km/sec) also dominate the northeastern region of the network with a few exceptions such as the Şenkaya area. Another distinct feature is the remarkable low velocity corridor along the 40° longitude ranging in between 5.6 km/sec and 5.7 km/sec and crossing the NAFZ vertically (Figure 5.14). The velocity change relative to the initial velocity model is approximately -8% (Figure 5.15) where the seismic activity is comparably lower. Unlike the other layers, relatively higher velocities were observed along the NAFZ. It should also be considered that the areas with reliable resolution are smaller compared to the shallower layers (Figure 5.15).

Majority of the earthquakes are located in the upper crust (up to 15 km) with a few exceptions. As a result, the velocity structure of the deepest grid layer at 20km is poorly resolved due to insufficient number of rays contributing the overall solution at this depth range as indicated by the synthetic data tests (Figure 5.9) and the resolution estimates such as RDEs (Figure 5.13). Accordingly, the reliable areas of high resolution are illustrated by a white contour in Figure 5.15 clearly indicating the lack of resolving power. Under these circumstances, it is hardly possible to make any sensible interpretation at 20km based on the inversion results shown in Figure 5.14 and 5.15.

Furthermore, the overall results relevant to the 1-D velocity inversions and the corresponding 3-D tomographic inversions should be interpreted both in terms of seismological and tectonic features of the target volume. In the following sub-sections, the results will be classified into two categories such as the updated hypocenter distribution and the resulting 3-D velocity structure for Eastern Turkey along the several vertical profiles. Sharp velocity gradients are an expression of horizontal and vertical discontinuities, revealing the location and the geometry of the faults.

5.5 Final Hypocenter Locations

The comparison of the final 3-D and the initial 1-D hypocenters are shown in Figure 5.16 along with the depth distribution. As mentioned in section 5.4 we observed a significant reduction (%50) both in data variance and residuals.

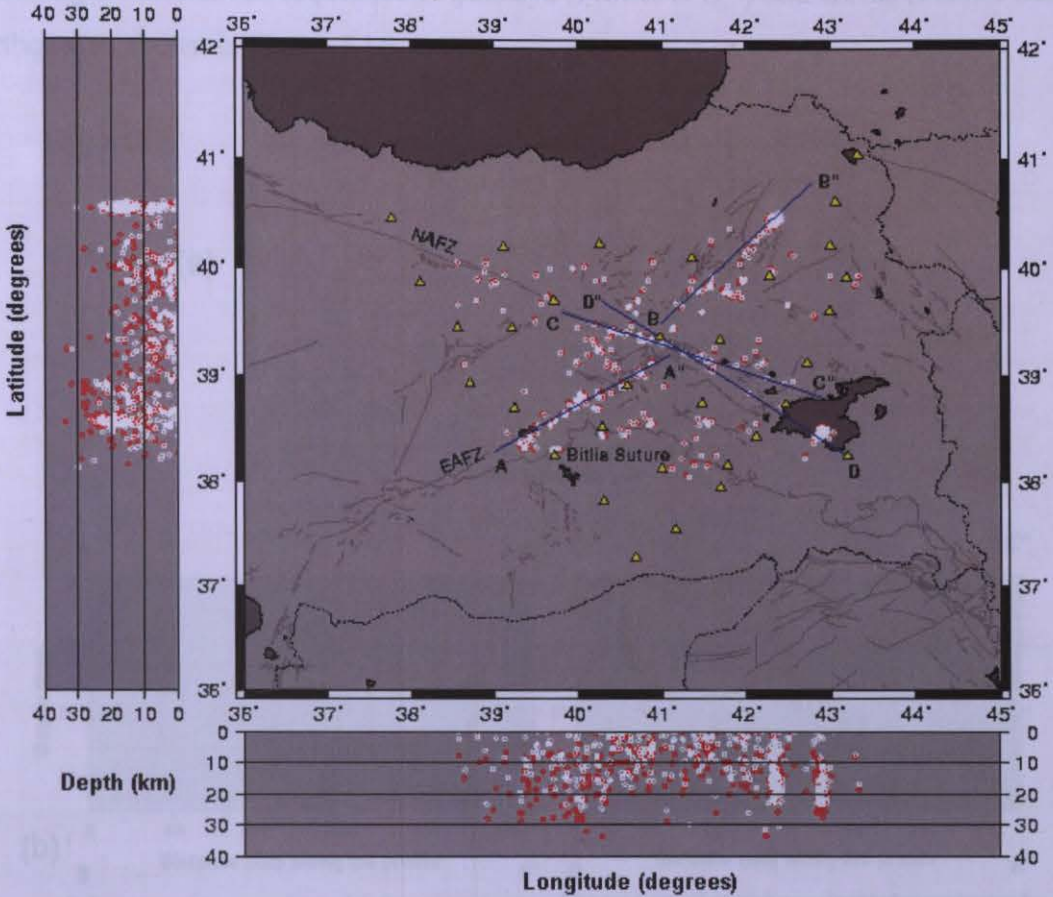


Figure 5.16. Initial and final hypocenter distribution after the 3-D inversion. Red and white circles denote the initial and the final hypocenters with the updated 3-D velocity model, respectively. Yellow triangles represent the stations and the blue lines denote the profiles.

S-wave velocities were directly calculated using the P-wave velocities and included in the hypocenter relocation process during the final stages of the 3-D inversion assuming *a priori* known average V_p/V_s value of 1.80 taking into account the study of Türkelli et al., (2003). S-phases provide useful information constraining the earthquake depths, which is also essential in the tomographic inversion process as stated in LET theory.

Figure 5.17 clearly illustrates the hypocenter distribution in horizontal and vertical directions where the displacement vectors including the initial locations were projected onto two parallel profiles along the major fault zones such as North Anatolian Fault Zone (NAFZ-Profile CC''), East Anatolian Fault Zone (EAFZ- AA''), and two profiles including the aftershock sequences of Şenkaya (Profile B-B'') and Gevaş (Profile DD'') earthquakes shown in Figure 5.16.

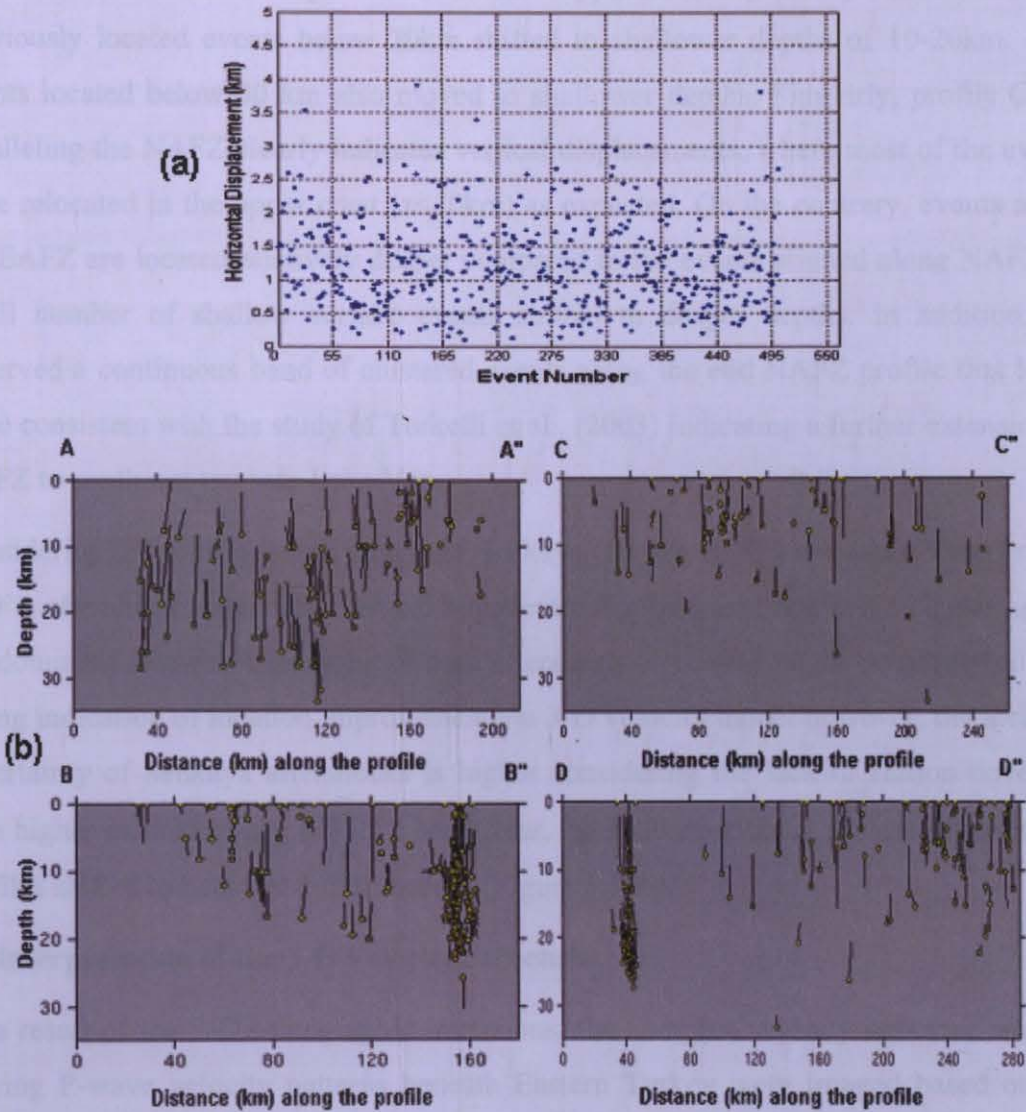


Figure 5.17. (a) Horizontal displacement of hypocenters. Blue dots represent the displacement values. (b) Comparison of the earthquake locations from the 1-D minimum velocity model and the 3-D model along 4 profiles (A-A'', B-B'', C-C'' and D-D''). Yellow circles represent the initial locations before the 3-D inversion. Displacement vectors are drawn to the final 3-D locations by thin lines.

3-D velocity model modified the earthquake locations both in vertical and horizontal directions to a certain extent. Majority of the horizontal hypocenter displacement in Figure 5.17(a) is in 0-2.5 km range with a few exceptions above 3km. With the use of the final 3-D velocity model, we observed a reduced hypocenter scattering especially along the EAFZ (Profile A-A'' in Figures 5.16 and 5.17b) where the hypocenters located 2-6 km away are relocated closely to the fault zone and aligned within the strike direction. The vertical displacement is also apparent along this profile where the previously located events below 20km shifted to shallower depths of 10-20km. Two events located below 30 km also moved to shallower depths. Similarly, profile C-C'' paralleling the NAFZ clearly indicates vertical displacements, where most of the events were relocated in the upper crust ($z < 10\text{km}$) as expected. On the contrary, events along the EAFZ are located relatively deeper compared to the events aligned along NAFZ. A small number of shallow surface events shifted to deeper depths. In addition, we observed a continuous band of clustered events along the end NAFZ profile that looks to be consistent with the study of Türkelli et al., (2003) indicating a further extension of NAFZ to southeast towards Lake Van.

Considering the profiles taken along the Şenkaya (Profile B-B'') and Lake Van (Profile D-D'') aftershock sequences, vertical hypocenter displacement and event clustering are the dominant features. Clustering of both aftershock sequences might be suggested as a strong indication of location improvement via 3-D velocity model however; the location uncertainty of Şenkaya aftershocks is higher considering the lack of station coverage with higher azimuthal gap ($\approx 170^\circ$). Moreover, the shallower surface events along these profiles shifted to between 1-5km deeper (Figure 5.17b).

5.6 Interpretation of the 3-D Velocity Structure

As a result of the 3-D tomographic inversions, the complex velocity structure and the varying P-wave velocity patterns beneath Eastern Turkey were imaged based on the careful analysis of the solution quality with synthetic tests and resolution estimates of the actual data (Sections 5.3 and 5.4) down to 20km depth depending on the source receiver distribution and the major tectonic features of the region. To interpret the results to a certain extent, a series of vertical depth cross-sections of the final 3-D V_p model were plotted perpendicular to the strike directions of the major fault systems such

as NAFZ, EAFZ and the aftershock sequences of the two mainshocks occurred during the ETSE project (Figure 5.16).

Vp profiles (A-A', B-B', C-C') taken perpendicular to EAFZ are shown in Figure 5.18.

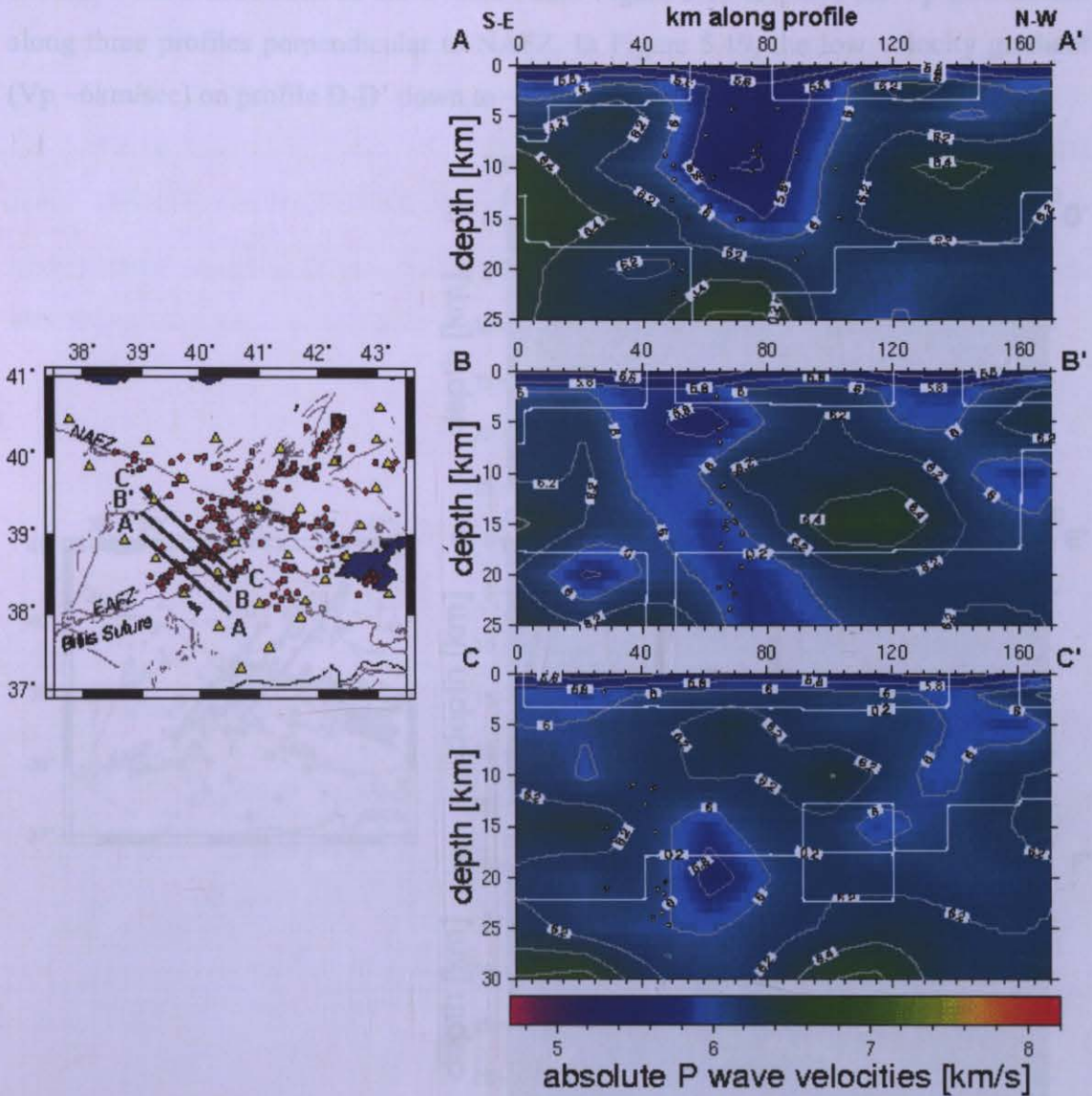


Figure 5.18. P-wave velocity distribution along three profiles (A-A', B-B', C-C') perpendicular to EAFZ. Areas of higher resolution are surrounded by a white contour (RDEs > 0.2). Vp values are contoured in every 0.2 km/sec interval.

In each figure where the profiles cross the EAFZ are marked by relatively lower velocities between 5.6 to 6.0 km/sec. Seismic activity is consistently concentrated in these weaker zones along EAFZ down to 15-17 km depth as expected. Because of degrading resolution below 17 km, we cannot resolve if the low Vp anomalies continue

to greater depth. Towards northwest, Vp values increase up to 6.4 km/sec indicating an undisturbed compact medium where no seismicity is detected. In Profile C-C', an area with lower velocities down 10-15 km depth were observed that might be caused by another weaker zone such as the Ovacik Fault. Figure 5.19 displays the Vp distribution along three profiles perpendicular to NAFZ. In Figure 5.19, the low velocity gradient (Vp ~6km/sec) on profile D-D' down to ~15km corresponds to the NAFZ between-

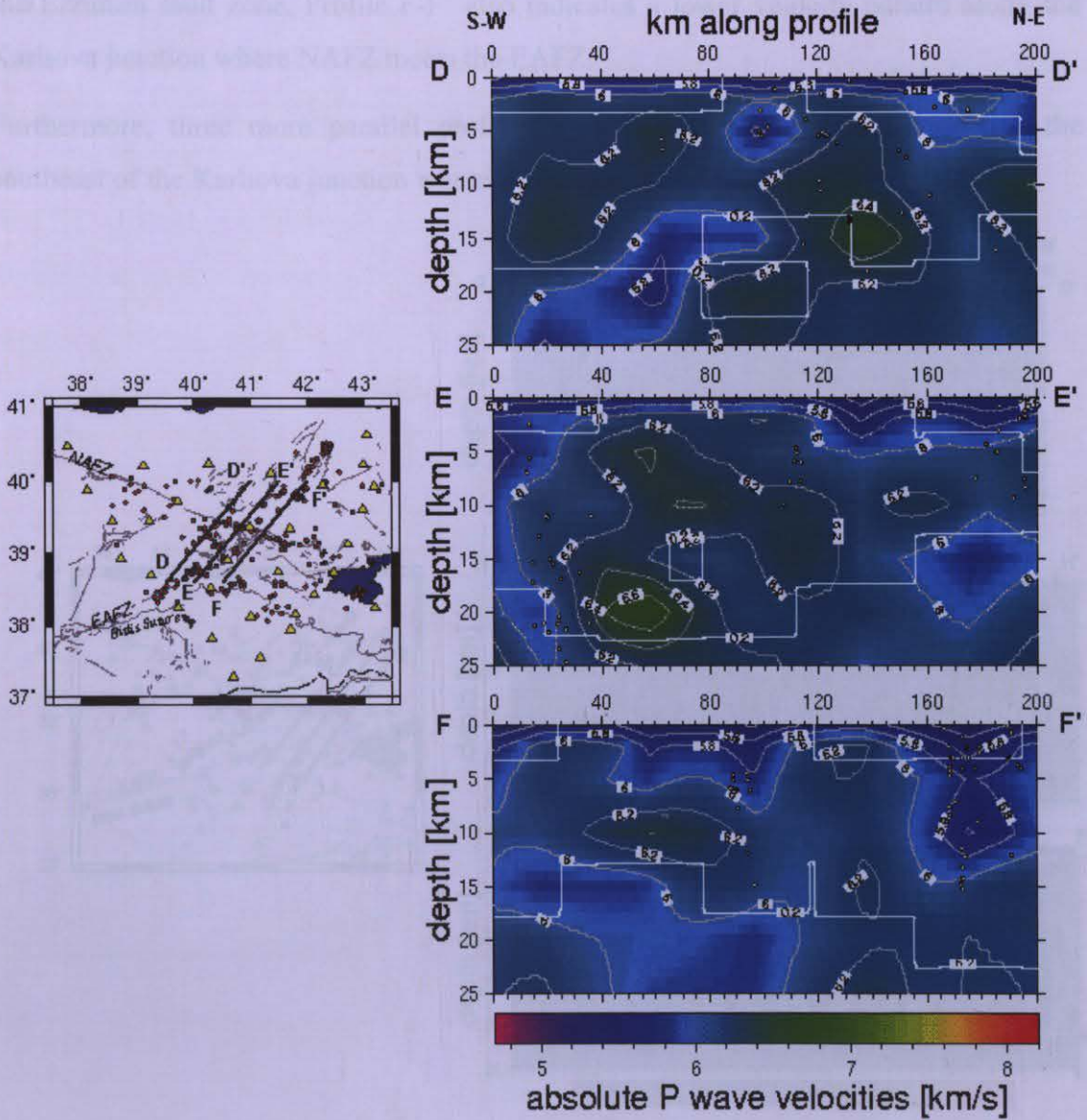


Figure 5.19. P-wave velocity distribution along three profiles (D-D', E-E', F-F') perpendicular to NAFZ. Areas of higher resolution are surrounded by a white contour (RDEs > 0.2). Vp values are contoured in every 0.2-km/sec intervals.

the 80th and the 120th km, which could also be observed along the other profiles (E-E' and F-F') in accordance to the more reliable areas of resolution. In addition, this distinctive feature looks to be well correlated with the observed seismicity. Higher velocity material is located towards the southeastern section of the profiles indicating sparse seismicity. A lower velocity anomaly of $V_p=5.8$ km/sec can be seen towards the end of profile F-F' that might be interpreted as another relatively weaker zone such as the Erzurum fault zone. Profile F-F' also indicates a lower velocity pattern along the Karliova junction where NAFZ meets the EAFZ.

Furthermore, three more parallel profiles were drawn in Figure 5.20 towards the southeast of the Karliova junction where seismicity continues in that direction.

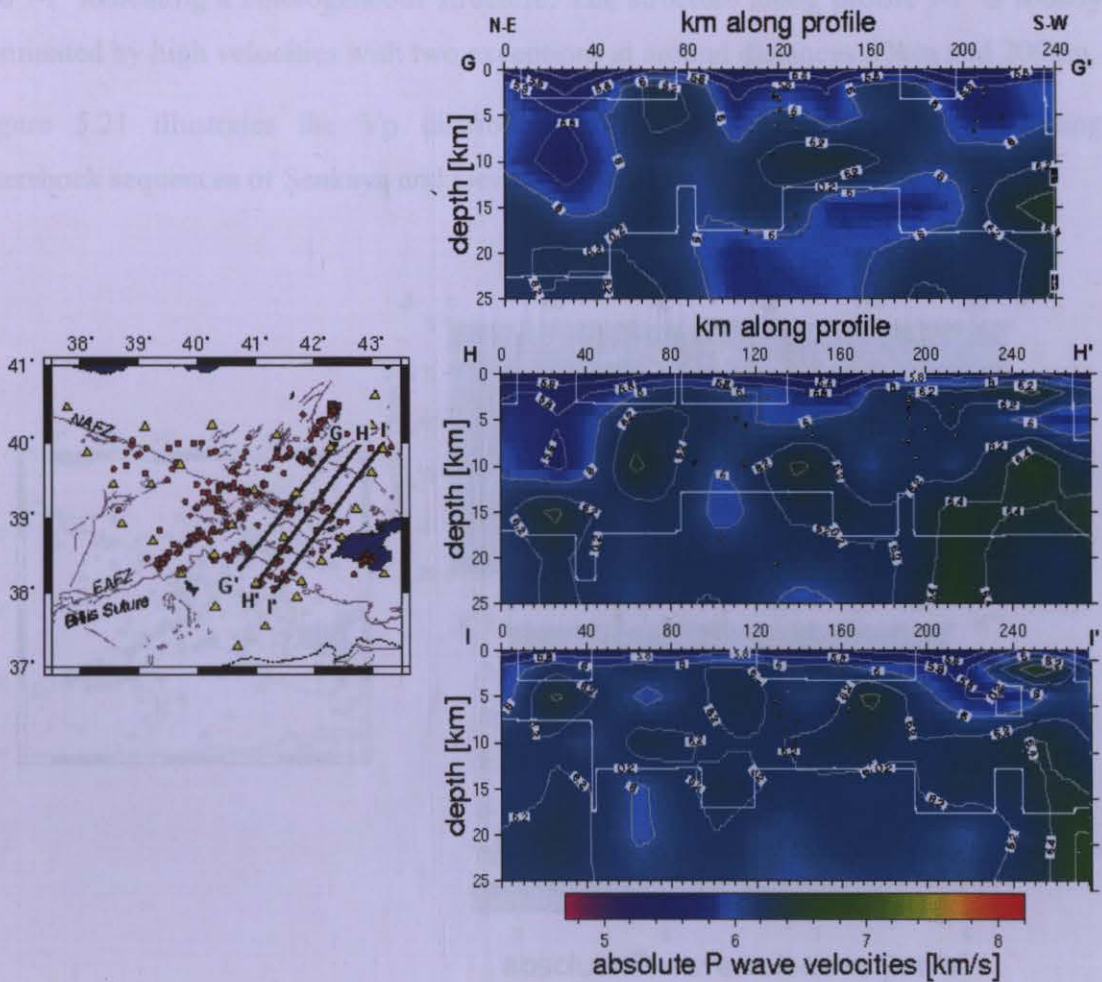


Figure 5.20. P-wave velocity distribution along three profiles (G-G', H-H', I-I'). Areas of higher resolution are surrounded by a white contour (RDEs > 0.2). V_p values are contoured in every 0.2-km/sec intervals.

In profiles G-G' and H-H', velocity variations appear to be quite similar indicating two distinct low velocity zones down to 10km depth consistent with the horizontal cross-sections in Figure 5.14. This weaker zone probably corresponds to Kağızman fault zone in both profiles. On the other hand, we do not recognize seismic activity around this fault. Another low velocity anomaly is located around the middle sections of the first two profiles that might tentatively be considered as the continuation of NAFZ towards southeast in accordance with the seismicity and the fault plane solutions (Örgülü and Aktar, 2003). Relatively higher velocities ($V_p \sim 6.2$ km/sec) were detected in between the two low velocity zones, also marked by sparse seismicity. Towards Bitlis thrust belt low velocities are apparent in profile G-G' but the situation is opposite in profile H-H' and I-I' indicating a heterogeneous structure. The structure along profile I-I' is mostly dominated by high velocities with two exceptions at around distances 50km and 200km. Figure 5.21 illustrates the V_p distribution along the vertical profiles including aftershock sequences of Şenkaya and Gevaş earthquakes.

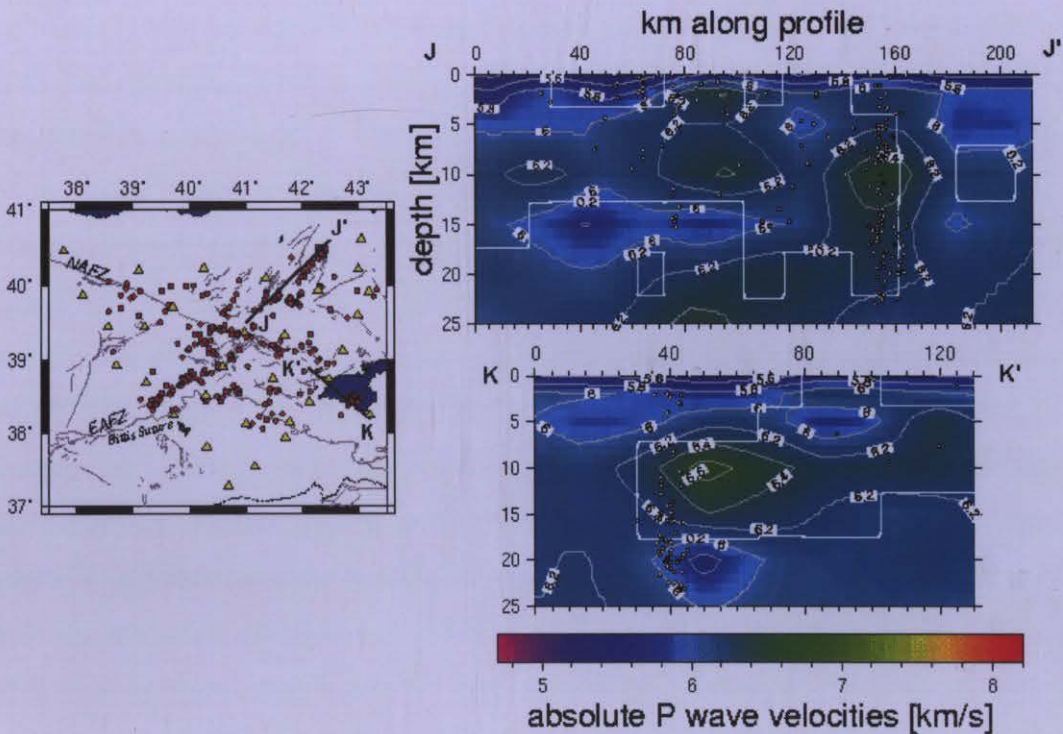


Figure 5.21. P-wave velocity distribution along three profiles (J-J', K-K'). Areas of higher resolution are surrounded by a white contour (RDEs > 0.2). V_p values are contoured in every 0.2-km/sec intervals.

Unlike the previous profiles, remarkably high velocities were observed along the profile J-J', which corresponds to the Şenkaya region. Relatively low velocity anomalies are located toward the beginning distances of the profile J-J' close to NAFZ. Seismic activity of the sequence is concentrated down to ~24 km depth with less location certainty. Resolution is fair compared to other profiles. Towards southwest transition from higher to lower velocities is recognizable but switches to higher velocities in further distances. In profile K-K' higher velocities ($6.2 < V_p < 6.4$ km/sec) are dominant around the area where the aftershocks of Gevaş earthquake are located. Depth ranges below 17 km is beyond our resolving power.

6 CONCLUSIONS

Local earthquake data from the Eastern Turkey Seismic Experiment (ETSE) has been used to construct three-dimensional (3-D) P-wave (V_p) tomographic images of the upper crustal structure beneath Eastern Turkey by local earthquake tomography (LET) method of Thurber (1983) and in particular, resulted in improved earthquake locations. Due to insufficient number of clear readings and high attenuation (Gök et al., 2003), S phases were not used in the simultaneous inversion but included in the earthquake relocation process. Depending on certain control parameters and model parametrization, careful analysis of solution quality with synthetic data sets and resolution estimates of actual data indicate that majority of the structural elements inside the station network are well resolved in ~ 3 -17 km depth range. Resolution dramatically decreased towards the outer parts of the network and below ~ 17 km depth.

3-D P-wave velocity model led to a more reliable hypocenter determination with a significant reduction of $\sim 50\%$ both in data variance and residuals compared to the study from Turkelli et al., (2003). Vast majority of the events along the major fault zones and the aftershock sequences of Gevaş and Şenkaya earthquakes shifted to shallower depths (5 km -15 km) with a few exceptions. We observed deeper events along the East Anatolian Fault Zone (EAFZ) relative to the events along the North Anatolian Fault Zone (NAFZ). Event depths in the upper crust are better constrained relative to the ones in the lower crust ($z > 20$ km). Accordingly, hypocenter scattering also reduced along the major fault zones (profiles in Figures 5.16 and 5.17) such as the NAFZ and EAFZ. Despite the heterogeneous hypocenter distribution in general, we observed increased clustering for the aftershock sequences. Hypocenter accuracy was found lower for Şenkaya aftershocks since the station coverage is not dense in that area. In our case, with the influence of improved velocity model, average location errors did not exceed ~ 1.5 km in horizontal and ~ 4 km in vertical directions indicating an overall improvement. Station corrections derived for the finalized 3-D velocity model are useful to help account for near-surface velocities and geology. 1-D velocity models are commonly used in routine location algorithms therefore; tomographic models can be informative and used for comparative studies.

3-D P-wave velocity distribution does not appear to be homogeneous in consistence with the seismicity. Tomographic images revealed the presence of lateral velocity variations along the horizontal and the vertical cross sections beneath the Anatolian Plateau since the continent-continent collision is taken up by strike-slip faulting (Örgülü and Aktar, 2003).

Existence of remarkably low velocity zones ($5.6 < V_p < 6.0$ km/sec) along most of the vertical profiles (Figures 5.18, 5.19, 5.20) indicates the influence of major tectonic structures such as NAFZ, EAFZ and the Bitlis thrust belt. These relatively weaker zones are possibly underlain by low velocity material where the seismic activity appears to be more intense and surrounded by higher velocities. Low velocity anomalies extend deeper along EAFZ (Figure 5.18) down to ~ 15 km compared to an approximate depth of 10km along NAFZ (Figure 5.19).

On the other hand, Arabian plate is generally marked by relatively higher velocities ($V_p > 6.2$ km/sec) in 10-15 km depth range (Figure 5.14 and the profile I-I' in Figure 5.20). Higher velocities were found in the Şenkaya and Gevaş mainshock areas (Figure 5.21). A dominant high velocity anomaly was observed along the profile K-K' where the majority of seismic activity is concentrated.

Moreover, besides the major fault zones, minor faults might also be detected by the profile C-C' (Figure 5.18) such as the Ovacık fault close to the city of Erzincan indicating V_p values of 6.0 km/sec and Çobandede fault along profile G-G' in Figure 5.20.

The challenge in displaying results from LET studies is the uneven distribution of information, with most detail near the seismically active fault zones, as discussed above. Regarding the LET studies, denser station spacing higher number of well locatable events inside the station network will definitely provide more accurate images of the major tectonic elements and earthquake source regions. Joint interpretation of the 3-D velocity structure and earthquake hypocenters is going to yield the most thorough and precise picture of active tectonic processes like faulting and type of deformation we can obtain from arrival time data to a certain extent.

REFERENCES

- Aki, K., 1982. Three-dimensional inhomogeneities in the lithosphere and asthenosphere: evidence for decoupling in the lithosphere and flow in the asthenosphere., *Rev. Geophys. Space Phys.*, 20, 161-170.
- Aki, K., and Lee, W.H.K., 1976. Determination of three-dimensional velocity anomalies under a seismic array using first P- arrival time from local earthquakes, 1. A homogeneous initial model, *J. Geophys. Res.*, 81, 4381-4399.
- Aki, K., Christofferson, A. and Husebye, E.S., 1976. Three-dimensional seismic structure of the lithosphere under Montana LASA, *Bull. Seismol. Soc. Am.*, 66, 501-524.
- Aki, K., Christofferson, A. and Husebye, E.S., 1977. Determination of the three dimensional seismic structure of lithosphere, *J. Geophys. Res.*, 82, 277-296.
- Aktar, M., Dorbath, C. and Arpat, E., 2004. The seismic velocity and fault structure of Erzincan basin, Turkey, using local earthquake tomography, *Geophys. J. Int.*, 156, 497-505.
- Al-Lazki, Ali I., Seber, D., Sandvol, E., Turkelli, N., Mohamad, R. and Barazangi, M., 2003. Tomographic Pn velocity and anisotropy structure beneath the Anatolian plateau (Eastern Turkey) and the surrounding regions, *Geophys. Res. Lett.*, 30 (24), 6, 1-4.
- Barazangi, M., 1989. Continental collision zones: Seismotectonics and crustal structure, in *Encyclopedia of Solid Earth Geophysics*, edited by D. James and V. Nostrand, Reinhold Company, New York, 58-75.
- Barka, A., and K. Kadinsky-Cade, 1988. Strike-slip fault geometry in Turkey and its influence on earthquake activity, *Tectonics*, 7, 663- 684.

- Barka, A., and R. Reilinger, 1997. Active tectonics of the eastern Mediterranean region: deduced from GPS, neotectonic and seismicity data, *Annali di Geofisica*, 40, 587-610.
- Clayton, R.W. and Comer, R.P., 1983. A tomographic analysis of mantle heterogeneities from body wave travel time (abstract), *Eos, Trans. Am. Geophys. Union*, 64, 776.
- Dewey, J. F., and A. M. C. Sengör, 1979. Aegean and surroundings regions: Complex multiplate and continuum tectonics in a convergent zone, *Geolog. Soc. of Amer. Bull.*, 90, 84-92.
- Dewey, J. F., M. R. Hempton, W. S. F. Kidd, F. Saroglu, and A. M. C. Sengor, 1986. Shortening of continental lithosphere: The neotectonics of eastern Anatolia— a young collision zone, in *Collision Tectonics*, edited by M. P. Coward and A. C. Ries, Geological Society Special Publications 19, 3 -36.
- Dziewonski, A.M. and Anderson, D.L., 1984. Seismic tomography of Earth's interior, *Am. Sci.*, 721, 483-394.
- Dziewonski, A.M., 1984. Mapping the lower mantle: determination of lateral heterogeneity in P velocity up to degree and order 6. *J. Geophys. Res.*, 89, 5929-5952.
- Eberhart-Phillips, D., 1986. Three-dimensional velocity structure in northern California Coast Ranges for inversion of local earthquakes arrival times, *Bull. Seismol. Soc. Am.*, 76, 1025-1052.
- Eberhart-Phillips, D., 1989. Investigations of crustal structure and active tectonic processes in the coast ranges, central California., Ph.D. Thesis, Stanford University, Stanford.
- Eberhart-Phillips, D., 1990. Three-dimensional P and S velocity structure in the Coalinga region., California., *J. Geophys. Res.*, 95, 15343-15363.
- Gök, R. , Sandvol, E., Türkelli, N., Seber, D., and Barazangi, M., 2003. Sn attenuation in the Anatolian and Iranian plateau and surrounding regions, *Geophys. Res. Lett.*, 30(24). 5,1-4.

Gök, R. , Türkelli, N., Sandvol, E., Seber, D., and Barazangi, M., 2000. Regional wave propagation in Turkey and surrounding regions. *Geophys. Res. Lett.*, 27(3) , 429-432.

Gürbüz, C., N. Turkelli, T. Bekler, R. Gok, E. Sandvol, D. Seber, and M. Barazangi, 2004. Location and calibration using eastern Turkey broadband seismic network: Analysis of the Ağrı Dam explosion, *Bull. Seism. Soc. Amer.*, 94,1166-1171.

Haslinger, F. and Kissling, E., 2001. Investigating effects of 3-D ray tracing methods in local earthquake tomography, *Phys.Earth planet.Inter.*,123, 103-114.

Haslinger,F., Kissling,E., Ansorge, J.,Hatzfeld D., Papadimitriou, E., Karakostas ,V., Makropoulos, K., Kahle, H.G. and Peter,Y., 1999. 3-D crustal structure from local earthquake tomography around the Gulf of Arta (Ionain region, NW Greece), *Tectonophysics*, 304, 210-218.

Hawley, B.W., Zandt, G. and Smith, R.B.,1981. Simultaneous inversion for hypocenters and lateral velocity variations: an iterative solution with layered model. *J.Geophys.Res.*,86,7073-7076.

Hirahara, K., 1977. A large-scale three-dimensional seismic structure under the Japan Islands and the Sea of Japan, *J. Phys. Earth*, 25, 393-417.

Husen S., Kissling, E. and Flueh,E.R.,2000.Local earthquake tomography of shallow subduction in north Chile:a combined onshore and offshore study , *J. Geophys. Res.*, 105, 28183-28198.

Husen S., Quintero,R., Kissling, E. and Hacker,B., 2003. Subduction zone structure and magmatic processes beneath Costa Rica constrained by local earthquake tomography and petrological modelling, *Geophys. J. Int.*,155,11-32.

Husen S., Smith R.B., Waite G.P., 2004. Evidence for gas and magmatic sources beneath the Yellowstone volcanic field from seismic tomographic imaging. *J. Volcanology and Geothermal Res.*, 131, 397-410.

Kaypak, B., Eyidođan, H., 2002. Erzincan Havzası 3-D hız yapısının yerel deprem tomografisi ile belirlenmesi (Doktora Tezi).

Jackson, J. A., and D. McKenzie, 1988. The relationship between plate motions and seismic moment tensors, and the rates of active deformation in the Mediterranean and Middle East, *Geophys. J.*, 93, 45– 73.

Keskin, M., J. A. Pearce, and J. G. Mitchell, 1998. Volcano-stratigraphy and geochemistry of collision-related volcanism on the Erzurum-Kars Plateau, North Eastern Turkey, *J. Volcanol. Geothermal Res.*, 85 (1 – 4), 355– 404.

Kissling, E., 1995. *Velest Users Guide*. Internal report, Institute of Geophysics, ETH Zurich, 26pp.

Kissling, E., Ellsworth, W.L., Eberhart-Phillips, D., Kradolfer, U., 1994. Initial reference models in seismic tomography. *J. Geophys. Res.* 99, 19635-19646.

Kissling, E., 1988. Geotomography with local earthquake data, *Rev. Geophys.*, 26, 659-698.

Kissling, E., Ellsworth, W.L., Eberhart-Phillips, D. and Kradolfer, U., 1994. Initial reference models in local earthquake tomography, *J. Geophys. Res.*, 99, 19635-19646.

Kissling, E., Husen S. and Haslinger, F., 2001. Model parameterization in seismic tomography: a choice of consequences for the solution quality, *Phys. Earth planet. Inter.*, 123, 89-101.

Lawson, C.L. and Hanson, R.J., 1974. *Solving Least Squares Problems*, Prentice- Hall, Englewood Cliffs. NJ.

Lienert, B. R., and J. Havskov, 1995. A computer program for locating earthquakes locally, regionally and globally, *Seismological Research Letters*, 66, 26– 36.

McClusky, S., S. Balassanian, A. Barka, C. Demir, S. Ergintav, I. Georgiev, O. Gurkan, M. Hamburger, K. Hurst, H. Kahle, K. Kastens, G. Kekelidze, R. King, V. Kotzev, O. Lenk, S. Mahmoud, A. Mishin, M. Nadariya, A. Ouzounis, D. Paradissis, Y. Peter, M. Prilepin, R. Reilinger, I. Sanli, H. Seeger, A. Tealeb, M. N. Toksöz, and G. Veis, 2000. GPS constraints on plate motion and deformation in the eastern Mediterranean: Implications for plate dynamics, *Journal of Geophysical Research*, 105, 5695– 5719.

McKenzie, D., 1972. Active tectonics of the Mediterranean region, *Geophys. J. R. Astr. Soc.*, 30(2), 109– 185.

Menke, W., 1989. *Geophysical Data Analysis: Discrete Inverse Theory*, Academic Press, Inc., San Diego.

Nolet, G., 1985. Solving or resolving inadequate and noisy tomographic systems, *J. Comput. Phys.*, 61, 463-482 .

Örgülü, G., M. Aktar, N. Türkelli, E. Sandvol, and M. Barazangi., 2003. Contribution to the seismotectonics of the Eastern Anatolian Plateau from moderate and small size events. *Geophys. Res. Lett.*, 30 (24), 3,1-4.

Pavlis, G.L. and Booker, J.R., 1980. The mixed discrete continuous inverse problem: Application to the simultaneous determination of earthquake hypocenters and velocity structure, *J. Geophysics. Res.*, 85, 4801-4810.

Pavlis, G.L. and Booker, J.R., 1983. A study of the importance of nonlinearity in the inversion of earthquake arrival time data for velocity structure, *J. Geophys. Res.*, 88, 5047-5055.

Pearce, J. A., J. F. Bender, S. E. De Long, W. S. F. Kidd, P. J. Low, Y. Güner, F. Saroglu, Y. Yilmaz, S. Moorbath, and J. G. Mitchell, 1990. Genesis of collision volcanism in Eastern Anatolia, Turkey, *Journal of Volcanology and Geothermal Research*, 44, 189–229.

Pereyra, V., Lee, W.H.K. and Keller, H.B., 1980. Solving two-point seismic raytracing problems in heterogeneous medium, Pt. 1. A general adaptive finite difference method, *Bull. Seismol. Soc. Am.*, 70, 79-99. NY.

Prothero, W.A., Taylor, W.J. and Eickemeyer, J.A., 1988. A fast, two – point, three dimensional ray tracing algorithm using a simple step search method. *Bull. Seismol. Soc. Am.*, 78, 1190-1198.

Rotstein, Y., and A. L. Kafka, 1982. Seismotectonics of the southern boundary of Anatolia, eastern Mediterranean region: Subduction, collision, and arc jumping, *Journ. Geophys. Res.*, 87, 7694–7706.

Sengör, A. M. C., and W. S. F. Kidd, 1979. Post-collisional tectonics of the Turkish-Iranian Plateau and a comparison with Tibet, *Tectonophysics*, 55, 361–376.

Thurber, C.H., 1983. Earthquake locations and three dimensional crustal velocity structure in the Coyote Lake area, central California. *J. Geophys. Res.* 88, 8226-8236.

Thurber, C.H., 1993. Local earthquake Tomography: velocities and V_p/V_s theory. In: Iyer, H.M., Hirahara, K. (Eds.), *Seismic Tomography: Theory and Practice*. Chapman and Hall, London, pp. 563-583.

Thurber, C.H., 1981. Earth Structure and Earthquake Locations in the Coyote Lake Area, Central California, Ph.D. Thesis, Massachusetts Institute of Technology, Cambridge, MA.

Thurber, C.H., 1983. Earthquake locations and three-dimensional crustal structure in the Coyote Lake area, central California., *J. Geophys. Res.*, 88, 8226-8236.

- Thurber, C.H., 1986. Analysis methods for kinematic data from local earthquakes., *Rev. Geophys.*, 24, 793-805.
- Toomey, D.R., and Foulger, G.R., 1989. Tomographic inversion of local earthquake data from the Hengill-Grensdalur central volcano complex, Iceland, *J. Geophys. Res.*, 94, 17497-17510.
- Türkelli, N., E. Sandvol, E. Zor, R. Gök, T. Bekler, A. Al-Lazki, H. Karabulut, S. Kuleli, T. Eken, C. Gürbüz, S. Bayraktutan, D. Seber, and M. Barazangi, 2003. Seismogenic Zones in Eastern Turkey, *Geophys. Res. Lett.*, 30 (24),
- Um, J., Thurber, C.H., 1987. A fast algorithm for two-point seismic ray tracing. *Bull. Seismol. Soc. Am.* 77, 972-986.
- Virieux, J., 1991. Fast and accurate ray tracing by Hamiltonian perturbation. *J. Geophys. Res.*, 96, 579-594.
- Virieux, J., and V. Arra, 1991. Ray tracing in 3-D complex isotropic media: An analysis of the problem, *Geophysics*, 59, 2057-2069.
- Wesson, R.L., 1971. Travel-time inversion for laterally inhomogeneous crustal velocity models, *Bull. Seismol. Soc. Am.*, 61, 729-746.
- Wielandt, E., 1987. On the validity of the ray approximation for interpreting delay times, in *Seismic Tomography*, pp. 85-98, Ed. Nolet, G., Reidel, Hingham, MA.
- Woodhouse, J.H. and Dziewonski, A.M., 1984. Mapping the upper mantle: Threedimensional modelling of earth structure by inversion of seismic waveforms, *J. Geophys. Res.*, 89, 5953-5986.
- Yilmaz, Y., 1990. Comparison of young volcanic associations of western and eastern Anatolia formed under a compressional regime: A review, *J. Volcanol. Geotherm. Res.*, 44, 69- 87.

Zhao, D., 1990. A tomographic study of seismic velocity structure in the Japan Islands, Ph.D Thesis, Tohoku University.

Zhao, D., Horiuchi, S. and Hasegawa, A., 1990. 3-D seismic velocity structure of the crust and the uppermost mantle in the northeastern Japan Arc. *Tectonophys.*, 181, 135-149.

Zor, E., Gürbüz C., Türkelli, N, Sandvol., E., Seber, D., Barazangi, M., 2003. The crustal structure of the East Anatolian Plateau from receiver functions. *Geophys. Res. Lett.*, (30) 24, 7, 1-4.